Emergence of unstable avoided crossing in the collective excitations of spin-1 spin-orbit-coupled Bose-Einstein condensates

Sanu Kumar Gangwar [1] Rajamanickam Ravisankar [2,3,*] Henrique Fabrelli [4]
Paulsamy Muruganandam [5] and Pankaj Kumar Mishra [1,†]

[1]*Department of Physics, Indian Institute of Technology, Guwahati 781039, Assam, India*
[2]*Department of Physics, Zhejiang Normal University, Jinhua, Zhejiang 321004, China*
[3]*Zhejiang Institute of Photoelectronics and Zhejiang Institute for Advanced Light Source,*
Zhejiang Normal University, Jinhua, Zhejiang 321004, China
[4]*Centro Brasileiro de Pesquisas Físicas, 22290-180 Rio de Janeiro, Rio de Janeiro, Brazil*
[5]*Department of Physics, Bharathidasan University, Tiruchirappalli 620024, Tamilnadu, India*

We present analytical and numerical results on the collective excitation spectrum of quasi-one-dimensional spin-orbit (SO)-coupled spin-1 spinor ferromagnetic Bose-Einstein condensates. The collective excitation spectrum, using Bogoliubov–de Gennes theory, reveals the existence of a diverse range of phases in the SO-coupling and Rabi coupling (k_L-Ω) planes. Based on the nature of the eigenvalue of the excitation spectrum, we categorize the k_L-Ω plane into three distinct regions, namely, I, II (IIa and IIb), and III. In region I, a stable mode with phononlike excitations is observed. In region IIa, single- and multiple-band instabilities are noted with a gapped mode, while multiband instability accompanied by a mode corresponding to no gap between low-lying and first-excited states is realized in region IIb, which also provides evidence of unstable avoided crossing between low-lying and first-excited modes, responsible for the I_o type of oscillatory nonequilibrium dynamical pattern formation. The gap between low-lying and first-excited states increases upon increasing the Rabi coupling and decreases upon increasing the SO coupling. Using eigenvector analysis, we confirm the presence of the spin-dipole mode in the spinlike modes in region II. We corroborate the nature of the collective excitation through real-time dynamical evolution of the ground state perturbed with the quench of the trap using the mean-field Gross-Pitaevskii model. This analysis suggests the presence of dynamical instability leading to the disappearance of the zeroth component of the condensate. In region III, mainly encompassing $\Omega \sim 0$ and finite k_L, we observe phononlike excitations in both the first-excited and the low-lying state. The eigenvectors in this region reveal alternative in- and out-of-phase behaviors of the spin components. Numerical analysis reveals the presence of a superstripe phase for small Rabi coupling in this region, wherein the eigenvector indicates the presence of more complicated spinlike-density mixed modes.

I. INTRODUCTION

Ultracold atoms offer a versatile but precise platform for exploring quantum matter in the presence of diverse synthetic fields [1]. The recent experimental realization of spin-orbit (SO) coupling in spinor ultracold atoms [2,3] has sparked great interest among researchers to explore the SO-coupling-related physics in large-spin systems, which is challenging to achieve in the electronic materials system of condensed-matter physics. Over the past few decades, research on spinor Bose-Einstein condensates (BECs) has captured the community's attention since it reveals interesting physical phenomena such as vortices [4], the turbulence state triggered by the modulational instabilities as a result of the counter-flow motion between binary components [5], quantum phase transitions [6,7], modulational instability [8], solitons [9], magnetized vector solitons [10], and supersolidlike behavior in quasi-two-dimensions [11].

In the field of ultracold gases, numerical simulations have become an indispensable tool for exploring numerous complex phases and the underlying detailed mechanisms that appear in those systems as low-lying excitation phases. To this end, the mean-field models based on Gross-Pitaevskii equations have been widely used to investigate various aspects of SO-coupled spinor BECs, such as phase separation [12], phase separation of vector solitons [13], stability and dynamics of solitons [14–16], spin precession, and separation between spin components owing to anomalous spin-dependent velocities [17–19]. Some studies have explored the dynamics of modulation instability [20], preparation of stripe states [21], and condensate flow past an obstacle [22] in SO-coupled BECs.

One of the intriguing features of the SO-coupled BECs is the presence of a modulated ground state that appears as stripe phases for high values of SO couplings [23,24]. In recent years, there have been several studies indicating an intimate connection between the stripe phase and the supersolid behavior of the BECs. For instance, Adhikari [11] reported supersolidlike states in quasi-two-dimensional

---
*Corresponding author: ravicpc2012@gmail.com
†Corresponding author: pankaj.mishra@iitg.ac.in

trapped SO-coupled spinor BECs. In multicomponent condensates, Goldstein and Meystre [25] initiated the study of the Hartree-Bogoliubov theory to determine the resulting quasiparticle frequency spectrum and observed the interference resulting from cross coupling among condensates leading to the reversal of the sign of two-body interaction, which triggers the onset of spatial instabilities. There are some studies that suggest domain formation through the dynamical stability analysis [26].

The investigation of collective excitations, which are low-lying excitations in BECs, has played a pivotal role in comprehending the fundamental characteristics of these quantum degenerate gases. This includes aspects such as the stability of various ground-state phases, superconductivity, and superfluidity [27,28]. Landau coined the term "excitations" to describe the emergence of superfluids as a combined effect of a weakly interacting mixture of phonon and roton quasiparticles. Subsequently, Bogoliubov employed Landau's excitation spectrum tools to explicate the superfluidity in BECs [29]. Experimentally, the realization of low-lying excitations has been achieved in dilute gases of rubidium [30] and sodium [31] atoms. For trapless spinor condensates, the study of collective excitations involved considering equal Rashba and Dresselhaus couplings. This investigation revealed the presence of maxon-roton excitations [32,33]. Utilizing Bragg spectroscopy, Khamehchi *et al.* provided experimental evidence of collective excitations by realizing roton-maxon modes in SO-coupled spinor systems [34].

Following the experimental realization of the collective excitation mode for SO-coupled BECs in the laboratory, a series of theoretical and numerical works was undertaken that revealed the more complex nature of these excitations. For instance, Chen *et al.* [35] demonstrated the collective excitation spectrum of Raman-induced SO-coupled spinor BECs confined in a quasi-one-dimensional (quasi-1D) harmonic trap. By tuning the Raman coupling strength, they projected the presence of three distinct phases: stripe, plane-wave, and zero-momentum phases. Additionally, they identified the spin-dipole and breathing modes of collective excitations, indicating clear phase boundaries. Numerical confirmation of these features was obtained through quench dynamics. Few studies indicate the presence of the plane-wave, zero-momentum, and stripe phases of the condensate as quadratic Zeeman coupling is introduced in the SO-coupled spin-1 BECs [36,37]. Ozawa *et al.* [38] numerically analyzed the dynamical and energetic instabilities of quasi-one-dimensional SO-coupled BECs. Ravisankar *et al.* [39] analytically and numerically analyzed the stability of the spin-$1/2$ binary SO-coupled BECs in quasi-two-dimensions using a collective excitation spectrum and found the presence of a phonon-maxon-roton mode in the spectrum for finite SO and Rabi couplings. Katsimiga *et al.* [40] analyzed the nonlinear solitary-wave excitation that appears in the form of different combinations of dark and bright solitons for the trapped spin-1 condensate in the harmonic trap. Subsequently, different sorts of vortex-bright-type excitations in the two-dimensional harmonically confined spin-1 BECs were also explored [41]. Rajat *et al.* [42] theoretically and numerically analyzed the collective excitation of SO-coupled spin-1 BECs in a cigar-shaped trap at both zero and finite temperature

and demonstrated the presence of density and spin excitation, which exhibits qualitatively different features at finite temperature than those at zero temperature.

So far, the studies of collective excitation in the spinor BECs have been mainly restricted to a specified range of coupling parameters. However, a comprehensive picture of the instabilities arising as a result of the collective excitation has been lacking. Moreover, from the dynamics point of view, it has been demonstrated that in the presence of finite detuning between the two spin states unstable avoided crossing [43,44] between the low-lying and first-excited states appears upon perturbation. Such a physical mechanism is responsible for constructing a class of oscillatory patterns I_o for dynamically oscillatory nonequilibrium pattern formation in quantum systems, which remains largely unexplored in the SO coupled spin-1 BECs along with linear Rabi coupling. In this paper we attempt to address these issues considering the ferromagnetic SO coupled spin-1 BECs by scanning a wide range of coupling parameters using analytical computation of the eigenspectrum and eigenvectors. Based on the detailed nature of the eigenspectrum, we divide the k_L-Ω plane into three regimes: (i) a stable region characterized by a phonon-like mode, (ii) unstable regimes broadly divided into two parts characterized by the presence of a gap (IIa) and gapless (IIb) behavior between the low-lying and first-excited spectra which also yields evidence of unstable avoided crossing modes, and (iii) a system exhibiting a phononlike symmetric maxon-roton mode for coupling values near $\Omega \sim 0$, which is also a mode corresponding to no gap between the low-lying and first-excited spectra. In the presence of a relatively small imaginary frequency, we observe both a weak instability and the emergence of a superstripe phase. In all the regions, we corroborate the analytical observation of the eigenspectrum with the real-time dynamics of the ground state using the Gross-Pitaevskii (GP) equations.

The paper is organized as follows. In Sec. II we present our theoretical model for investigating the collective excitations and instabilities of SO-coupled spin-1 ferromagnetic BECs. Section III illustrates the single-particle spectrum, followed by the analysis of the collective excitation spectrum using the Bogoliubov–de Gennes theory in Sec. IV. In Sec. V we analytically and numerically report the collective excitation spectrum, identifying various stability regions. Section V provides the excitation spectrum and corresponding dynamical observations using the GP equations. Section VI summarizes the findings.

II. MEAN-FIELD MODEL

We consider a quasi-1D spin-1 spinor SO-coupled BECs realized by tight confinement in the transverse direction [45]. The nondimensional dynamical equations for quasi-1D SO-coupled spin-1 BECs are given by [14,40,46,47]

$$i\frac{\partial \psi_{\pm 1}}{\partial t} = \left(-\frac{1}{2}\frac{\partial^2}{\partial x^2} + V + c_0\rho\right)\psi_{\pm 1} \mp \frac{k_L}{\sqrt{2}}\frac{\partial \psi_0}{\partial x}$$
$$+ c_2^{\pm}\psi_{\pm 1} + \psi_0^2\psi_{\mp 1}^* + \frac{\Omega}{\sqrt{2}}\psi_0, \tag{1a}$$

$$i\frac{\partial \psi_0}{\partial t} = \left(-\frac{1}{2}\frac{\partial^2}{\partial x^2} + V + c_0\rho\right)\psi_0 + \frac{k_L}{\sqrt{2}}\left(\frac{\partial \psi_{+1}}{\partial x} - \frac{\partial \psi_{-1}}{\partial x}\right)$$

$$+ c_2^0\psi_0 + 2\psi_0^*\psi_{+1}\psi_{-1} + \frac{\Omega}{\sqrt{2}}(\psi_1 + \psi_{-1}), \quad (1b)$$

where $c_2^\pm = (\rho_{\pm 1} + \rho_0 - \rho_{\mp 1})$, $c_2^0 = (\rho_{+1} + \rho_{-1})$, and ψ_j ($j = +1, 0, -1$) are the spinor condensate wave functions that satisfy the normalization condition $\int_{-\infty}^{\infty}\rho\, dx = 1$, where $\rho_j = |\psi_j|^2$ and $\rho = |\psi_{+1}|^2 + |\psi_0|^2 + |\psi_{-1}|^2$. The dimensionless equations (1a) and (1b) are obtained with nondimensionalized time, length, and energy with respect to ω^{-1}, $l_0 = \sqrt{\hbar/m\omega}$, and $\hbar\omega$, respectively, where $\omega = \omega_x$ is the trap frequency along the x axis. The resulting condensate wave function takes the form $\psi_j = \sqrt{\frac{l_0}{N}}\tilde{\psi}_j$, where N is the total number of atoms. In addition, $V(x) = x^2/2$ is the trap potential, $c_0 = 2Nl_0(a_0 + 2a_2)/3l_\perp^2$ is the density-density interaction strength, and $c_2 = 2Nl_0(a_2 - a_0)/3l_\perp^2$ is the spin-exchange interaction strength with a_0 and a_2 the s-wave scattering lengths in the total spin channels 0 and 2, respectively. The nature of the interaction strength depends on the sign of c_2: $c_2 < 0$ represents the ferromagnetic condensate, while $c_2 > 0$ denotes the antiferromagnetic condensate [47,48]. Here $l_\perp = \sqrt{\hbar/m\omega_\perp}$ is the harmonic-oscillator length in the transverse direction with $\omega_\perp = \sqrt{\omega_y\omega_z}$. The SO- and Rabi-coupling strengths are given by $k_L = \tilde{k}_L/\omega_x l_0$ and $\Omega = \tilde{\Omega}/\hbar\omega_x$, respectively. In the above description, the quantities with a tilde represent dimensional quantities.

One important entity that characterizes the miscibility of different spin components is the magnetization of spin-1 spinor condensates defined by

$$\mathcal{M} = \int_{-\infty}^{\infty}[\rho_{+1}(x) - \rho_{-1}(x)]dx. \quad (2)$$

The energy functional corresponding to the coupled GP equations (1a) and (1b) is given by [12,49]

$$E = \frac{1}{2}\int_{-\infty}^{\infty}dx\left(\sum_j |\partial_x\psi_j|^2 + 2V(x)\rho + c_0\rho^2\right.$$

$$+ c_2[\rho_{+1}^2 + \rho_{-1}^2 + 2(\rho_{+1}\rho_0 + \rho_{-1}\rho_0 - \rho_{+1}\rho_{-1}$$

$$+ \psi_{-1}^*\psi_0^2\psi_{+1}^* + \psi_{-1}\psi_0^{*2}\psi_{+1})] + \sqrt{2}\Omega[(\psi_{+1}^* + \psi_{-1}^*)\psi_0$$

$$+ \psi_0^*(\psi_{+1} + \psi_{-1})] + \sqrt{2}k_L[(\psi_{-1}^* - \psi_{+1}^*)\partial_x\psi_0$$

$$\left.+ \psi_0^*(\partial_x\psi_{+1} - \partial_x\psi_{-1})]\right). \quad (3)$$

In order to make the set of dimensionless parameters used for our simulations viable for an experiment, here we outline the dimensional experimental parameters. For the ferromagnetic system, we consider ^{87}Rb BECs with the number of atoms $N \sim 2 \times 10^4$. The axial trap frequency is $\omega_x = 2\pi \times 50$ Hz, while the transverse trap frequencies are considered to be $\omega_y = \omega_z = 2\pi \times 500$ Hz. The spin-dependent and spin-independent interactions can be achieved by controlling the s-wave scattering lengths through Feshbach resonance; by varying the magnetic field, we can tune the s-wave scattering lengths [50–52]. We can achieve the SO-coupling strengths

in the range of $k_L = 0.1$–5 by changing the laser wavelengths from 68.86 μm to 1377.22 nm. Further, we can also control the Rabi coupling strength in a similar range by changing the frequency of the laser from $2\pi\hbar \times 5$ Hz to $2\pi\hbar \times 250$ Hz.

III. SINGLE-PARTICLE SPECTRUM

In this section we present the single-particle spectrum [10,53,54] of the noninteracting spinor condensate for trapless SO- and Rabi-coupled spin-1 spinor BECs. Following that, we introduce the collective excitation spectrum for the interacting systems.

For $V(x) = 0$ and $c_0 = c_2 = 0$, substituting $\psi_{0,\pm 1} = \phi_{0,\pm 1}e^{i(q_x x - \omega t)}$ in Eqs. (1a) and (1b), we obtain

$$\mathcal{L}_{sp}\begin{pmatrix}\phi_1 \\ \phi_0 \\ \phi_{-1}\end{pmatrix} = \omega\begin{pmatrix}\phi_1 \\ \phi_0 \\ \phi_{-1}\end{pmatrix}, \quad (4)$$

with

$$\mathcal{L}_{sp} = \frac{1}{2}\begin{pmatrix}q_x^2 & L & 0 \\ S & q_x^2 & L \\ 0 & S & q_x^2\end{pmatrix}, \quad (5)$$

where $L = -\sqrt{2}(ik_L q_x - \Omega)$ and $S = \sqrt{2}(ik_L q_x + \Omega)$. Upon diagonalizing Eq. (4), we obtain the single-particle spectrum as

$$\omega_0 = \frac{q_x^2}{2}, \quad (6a)$$

$$\omega_\pm = \frac{1}{2}\left(q_x^2 \pm 2\sqrt{\Omega^2 + k_L^2 q_x^2}\right). \quad (6b)$$

From Eqs. 6(a) and 6(b) it is quite evident that the single-particle spectrum exhibits three branches, namely, ω_0 and $\omega_\pm$. Among them, ω_0 is independent of SO and Rabi couplings, a constant branch of the single-particle spectrum. However, the detailed nature of the other two branches $\omega_\pm$ depends on the SO and Rabi couplings, which are designated as positive and negative branches of the spectrum, respectively, throughout the paper.

To start with, we consider both the SO (k_L) and Rabi (Ω)-coupling strengths as zero. We obtain the nondegenerate parabolic spectrum of the SO-coupled spin-1 system as couplings are set to zero [see Fig. 1(a)]. As ω_0 of the spectrum is independent of both the SO and Rabi couplings, it does not show any change upon the variation of coupling strengths, as shown in Figs. 1(a)–1(e) with the green dash-dotted line. To understand the behavior of the positive branch ω_+ and negative branch ω_- of the single-particle spectrum, we introduce the finite value of SO coupling in the absence of Rabi coupling and vice versa. First, we introduce a finite value to the SO-coupling strength $k_L = 0.7$ in the absence of Rabi-coupling strength $\Omega = 0.0$. For this parameter, the negative branch of the spectrum gets transformed from the parabolic to a double minimum, which appears at $q_x = \pm k_L$, as shown in Fig. 1(b). Here the energy minima of $\omega_- = -0.245$ occur at $q_x = \pm 0.7$. As Rabi coupling is increased to a finite value $\Omega = 0.5$ while keeping $k_L = 0.0$, we find a change from a double minimum to a single minimum ($\Omega > k_L^2$), which leads to a gap between the ω_+ and ω_0 branches. The magnitude of the gap between the ω_+ and ω_0 branches and between the ω_0 and ω_- branches
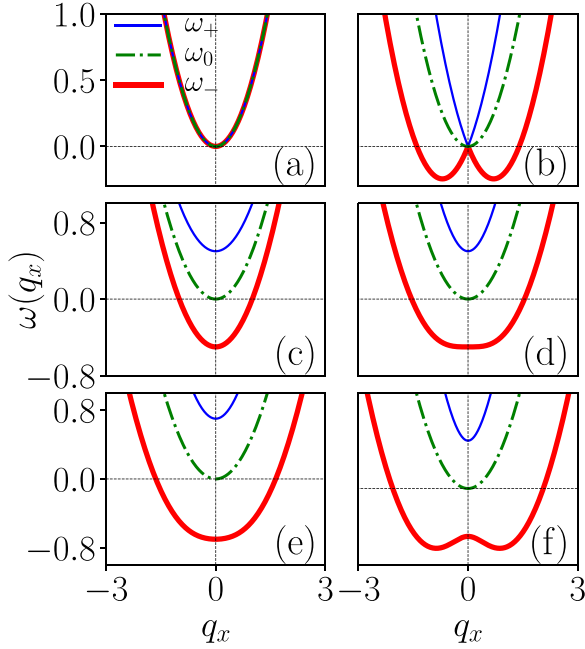
FIG. 1. Single-particle energy spectrum in momentum space for different sets of SO- and Rabi-coupling strengths (k_L, Ω): (a) $(0, 0)$, (b) $(0.7, 0)$, (c) $(0, 0.5)$, (d) $(0.7, 0.5)$, (e) $(0.7, 0.7)$, and (f) $(1.0, 0.5)$. The thick red solid, green dash-dotted, and thin blue solid lines represent the energy eigenspectrum for the $\{-1, 0, +1\}$ components of the spin, respectively. Varying the coupling parameters leads to the changes in the eigenspectrum of different components, that is, ω_- has only the lowest minimum for $\Omega > k_L^2$, whereas for $\Omega < k_L^2$ the ω_- exhibits double minima of the plane-wave phase, indicating the presence of the stripe phase.

is of the order of Ω. It appears to be of the order of 2Ω between the ω_+ and ω_- branches, as shown in Fig. 1(c), which exhibits a single minimum with $\omega_- = -0.5$ at $q_x = 0$. Further, we analyze the spectrum by introducing both couplings strengths, i.e., $k_L = 0.7$ and $\Omega = 0.5$, for which we obtain the global minima in the spectrum, which also satisfies the condition $\Omega \approx k_L^2$. Upon increasing the Rabi coupling value from $\Omega = 0.5$ to $\Omega = 0.7$, we obtain a similar kind of spectrum, but the gap between the branches increases with an increase in Rabi coupling, as shown in Figs. 1(d) and 1(e), with energies

$\omega_- = -0.5$ and $\omega_- = -0.7$ at $q_x \approx 0.0$. On the other hand, upon increasing the SO coupling from $k_L = 0.7$ to $k_L = 1.0$, we obtain the transition of single-minimum nature of ω_- into a double minimum, as shown in Fig. 1(f). At a later stage, we will see that this feature (the occurrence of a double minimum) in the single-particle spectrum is responsible for the appearance of the stripe phase in the situation when $\Omega < k_L^2$. In Fig. 1(f) the lowest-energy minimum is $\omega_- = -0.625$ at $q_x \approx \pm 0.9$. We observe that when $\Omega > k_L^2$ the energy depends on only the Rabi coupling, while if $\Omega < k_L^2$ the energy depends on the SO-coupling strength. Overall, we find that, upon variation of SO coupling, the positive branch exhibits a single minimum upon fixing the Rabi coupling at a finite value. However, the negative branch exhibits a transition from the single minimum to a double minimum upon varying the SO coupling, keeping the Rabi coupling fixed. This typical feature of the negative branch of the spectrum appears to indicate the change in the phases of the condensate upon varying the coupling parameters; therefore, for later discussion, we focus on analyzing the typical features of the ω_- branch.

In the next section we discuss the effect of both coupling terms (SO and Rabi) on the collective excitation spectrum for the interacting SO- and Rabi-coupled spin-1 BECs.

IV. BOGOLIUBOV–DE GENNES ANALYSIS OF THE COLLECTIVE EXCITATION SPECTRUM

In the preceding section we discussed the single-particle spectrum of SO-coupled spin-1 ferromagnetic BECs. In this section we present the collective excitation spectrum of the uniform condensate using the Bogoliubov–de Gennes (BdG) analysis. The excitation wave function in terms of the perturbation term $\delta\phi_j$ and uniform ground-state wave function ϕ_j can be represented as [22,25]

$$\psi_j(x, t) = e^{-i\mu_j t}[\phi_j + \delta\phi_j(x, t)], \tag{7}$$

where

$$\delta\phi_j(x, t) = u_j e^{i(q_x x - \omega t)} + v_j^* e^{-i(q_x x - \omega^* t)} \tag{8}$$

is the ground-state wave function with $\phi_j = (1/2, -1/\sqrt{2}, 1/2)^T$. Here μ_j denotes the chemical potential and u_j and v_j are the Bogoliubov amplitudes, with $j = +1$, 0, and -1 corresponding to the three components of spinor density of condensates. Substituting Eq. (7) in the dynamical equations (1a) and (1b), we obtain

$$\mathcal{L}(u_{+1} \ v_{+1} \ u_0 \ v_0 \ u_{-1} \ v_{-1})^T = \omega(u_{+1} \ v_{+1} \ u_0 \ v_0 \ u_{-1} \ v_{-1})^T, \tag{9}$$

where T represents the transpose of the matrix and $\mathcal{L}$ is 6×6 matrix given by

$$\mathcal{L} = \begin{pmatrix} H_+ - \mu_+ & \mathcal{L}_{12} & \mathcal{L}_{13} & \mathcal{L}_{14} & \mathcal{L}_{15} & \mathcal{L}_{16} \\ \mathcal{L}_{21} & -H_+ + \mu_+ & \mathcal{L}_{23} & \mathcal{L}_{24} & \mathcal{L}_{25} & \mathcal{L}_{26} \\ \mathcal{L}_{31} & \mathcal{L}_{32} & H_0 - \mu_0 & \mathcal{L}_{34} & \mathcal{L}_{35} & \mathcal{L}_{36} \\ \mathcal{L}_{41} & \mathcal{L}_{42} & \mathcal{L}_{43} & -H_0 + \mu_0 & \mathcal{L}_{45} & \mathcal{L}_{46} \\ \mathcal{L}_{51} & \mathcal{L}_{52} & \mathcal{L}_{53} & \mathcal{L}_{54} & H_- - \mu_- & \mathcal{L}_{56} \\ \mathcal{L}_{61} & \mathcal{L}_{62} & \mathcal{L}_{63} & \mathcal{L}_{64} & \mathcal{L}_{65} & -H_- + \mu_- \end{pmatrix}. \tag{10}$$
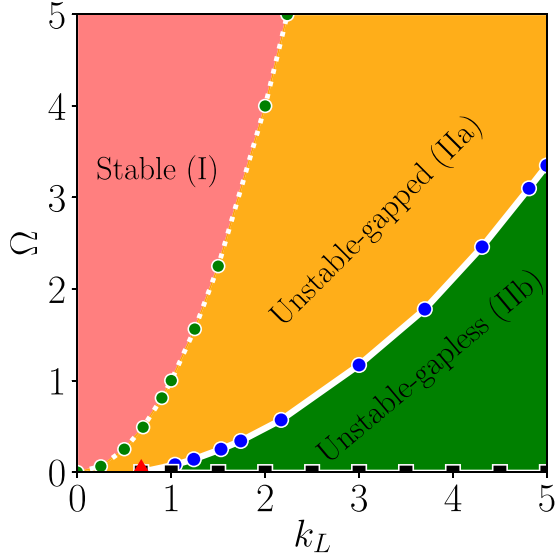
FIG. 2. Stability phase diagram in the k_L-Ω plane for the interaction parameters $c_0 = 0.5$ and $c_2 = -0.1$, which are considered for all the simulation runs. Based on the different characteristics of the eigenspectrum and ground state, the phase diagram is divided into regions I, IIa, IIb, and III. While region I is stable, regions IIa, IIb, and III are unstable. The white dotted line with green circles represents the $\Omega = k_L^2$ curve that separates region I from IIa. The white solid line with blue circles represents $\Omega \approx 0.1365k_L^2 - 0.0686$, which separates regions IIa and IIb. The horizontal line with rectangles for $\Omega \sim 0$ denotes the region III after the cutoff, $k_L^c = 0.68$, which is a tricritical point for regions IIa, IIb, and III, indicated by a red triangle.

The matrix elements of $\mathcal{L}$ are given in Appendix A. Bogoliubov coefficients follow the normalization condition

$$\int \left(\sum_j (|u_j|^2 - |v_j|^2) \right) dx = 1. \tag{11}$$

The simplified form of the BdG excitation spectrum is obtained by calculating the determinant of the matrix $\mathcal{L}$ and equating it with zero, i.e., $\det(\mathcal{L} - \omega I) = 0$, where I is a 6×6 identity matrix. The characteristic equation can be written as

$$\omega^6 + b\omega^4 + c\omega^2 + d = 0, \tag{12}$$

where the coefficients of b, c, and d are given in Appendix A.

V. EFFECT OF RABI AND SO COUPLING ON THE EXCITATION SPECTRUM

To better understand the stability of the ground-state phases of the system, we plot the stability diagram of the system in the k_L-Ω plane with interaction parameters $c_0 = 0.5$ and $c_2 = -0.1$ [55]. We obtain the stability phase plot by solving the collective excitation spectrum. The real frequencies of the BdG matrix imply the dynamically stable phase while the imaginary frequency indicates a dynamically unstable phase [25,38,39,47,56]. In Fig. 2 we show the stability diagram in the k_L-Ω plane. Based upon the eigenvalue, the plane is divided mainly into three regions, viz., stable region I and unstable regions II and III. The white dotted line with green

circles separates the stable and unstable regions, which have the phase transition boundary, i.e., $\Omega = k_L^2$ [39]. Further, we divide the unstable region into two separate parts: regions IIa and IIb. The white solid line with blue circles separates regions IIa and IIb. The critical points for the phase transition from region IIa to region IIb can be obtained by a polynomial fit given by $\Omega \approx 0.1365k_L^2 - 0.0686$. In region IIa we obtain a clear gap between the low-lying (negative branch) and first-excited (positive branch) branches of the spectrum. Also, for a fixed value of the Rabi-coupling strength Ω, upon increasing the SO-coupling strength k_L, the number of instability bands changes from 1 to 2 or vice versa. In region IIb we obtain overlap among the low-lying (ll) and first-excited (fe) branches of the eigenspectrum. Thus, the line delineates regions IIa and IIb, encompassing points where instability is present by means of multiple instability bands and gap openings between low-lying and first-excited states. Furthermore, in region IIb we observe a spectrum characterized by multiple instability bands. In this region for a fixed value of the Rabi-coupling strength Ω, upon increasing the SO-coupling strength k_L, we achieve a mode corresponding to no gap between the low-lying and first-excited branches of the spectrum for some range of quasimomentum. By increasing the Rabi-coupling strength with fixed SO coupling, we can again achieve the gapped mode between the low-lying and first-excited branches.

The transition from region IIa to region IIb can be obtained after a certain critical coupling point. We obtain the gapless behavior of the eigenspectrum by either increasing SO coupling ($k_L > k_L^c$) for a fixed Rabi coupling ($\Omega > \Omega^c$) or decreasing Rabi coupling ($\Omega^c < \Omega$) for a fixed SO coupling ($k_L > k_L^c$), with the critical coupling parameters $k_L^c = 0.68$ and $\Omega^c = 0.001$. This point is the origin of the line which separates regions IIa and IIb. At the horizontal line where the Rabi-coupling strength is approximately zero ($\Omega \approx 0.0$), we realize the presence of a phonon mode in the low-lying branch as well as in the first-excited branch of the spectrum, along with the presence of an instability band. These features in IIa and IIb are completely different from those obtained for region I. The cutoff value of the SO-coupling strength to obtain this behavior along the line is $k_L^c = 0.68$. We analyze the behavior of the system along the horizontal line separately in region III. Here k_L^c is the tricritical point for regions IIa, IIb, and III, which is indicated by the red triangle in the phase plot (see Fig. 2). Based on the above observations, we divide the phase plot into three different regions: regions I, II (consisting of parts IIa and IIb), and III. In Appendix C we show a similar kind of phase diagram for two other different sets of interaction strengths $c_0 = 5.0$ and $c_2 = -0.1$, and $c_0 = 885.72$ and $c_2 = 4.09$. With these interactions, we obtain phase plots (see Appendix B) similar to those in Fig. 2.

As we divide the phase diagram of the k_L-Ω plane into three regions, we discuss their behavior in each region individually. The detailed structure of the presentation in different regions is as follows. We perform collective excitation spectrum calculations to understand the stability of the system both dynamically and energetically. Real but negative eigenfrequencies of the BdG matrix suggest an energetically unstable nature of the condensate, while complex eigenfrequencies indicate a dynamically unstable nature of the condensate
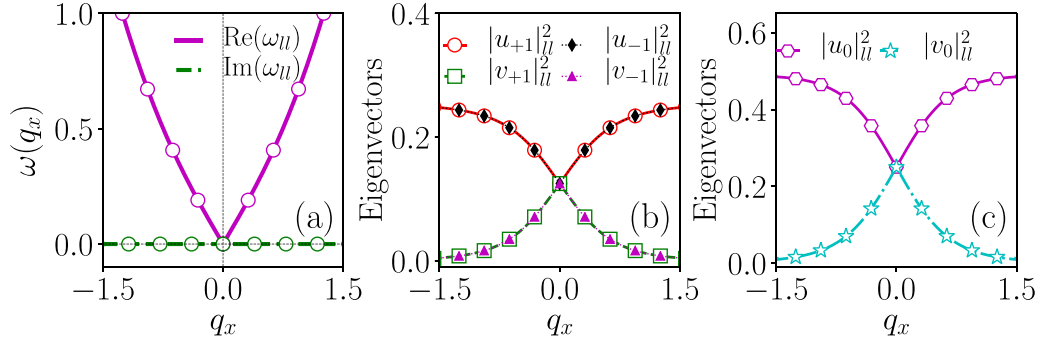
FIG. 3. (a) Excitation spectrum and (b) and (c) eigenvectors for the coupling parameters $k_L = 0.5$ and $\Omega = 2.0$. (a) The magenta solid line represents $\mathrm{Re}(\omega_-)$ and the green dash-dotted line represents $|\mathrm{Im}(\omega_-)|$. Here solid and dash-dotted lines are the analytical results of the BdG equation (12) and open circles are numerical results obtained by solving Eq. (9). (b) and (c) Eigenvectors corresponding to the eigenspectrum, obtained by solving Eq. (9) numerically: $|u_{+1}|^2$ (open red circles), $|u_{-1}|^2$ (closed black diamonds), $|u_0|^2$ (open magenta hexagons), $|v_0|^2$ (open cyan stars), $|v_{+1}|^2$ (open green squares), and $|v_{-1}|^2$ (closed magenta triangles). The presence of the phonon mode in the eigenspectrum is shown in (a). It has no negative or complex eigenfrequency and thus it is energetically and dynamically stable.

[38,47,49]. To validate these claims, we perform numerical simulations using the GP equations. We provide the eigenvalue spectrum, eigenvectors, and numerical simulation in each section.

Following this, we corroborate the analytical results for the excitation spectrum by numerically solving the BdG equation (10) from which we also obtain the eigenvectors as a function of q_x. First we consider a $[-1000, 1000]$ grid in real space with step size $h_x = 0.2$. Then we use the Fourier collocation method, where we numerically compute the Fourier transform of the BdG equations and obtain a truncated reduced BdG matrix, which is subsequently diagonalized using the LAPACK package [57]. In momentum space, we consider $[-700, 700]$ modes in the q_x direction, with a grid step size of $h_{q_x} = 0.0157$.

Further, we provide an analysis of the real-time dynamics corresponding to the collective excitation spectrum by solving the coupled GP equations (1a) and (1b) numerically. We use the imaginary-time-propagation method to obtain the ground state. Then we evolve the ground state in time using the real-time-propagation method. For this purpose, we adopt the split-step Crank-Nicholson scheme outlined in Refs. [49,58,59]. We consider a grid of 1280 space points with space step $dx = 0.05$ and time step $dt = 0.000\,25$ for imaginary-time propagation and $dt = 0.0005$ for real-time propagation. Initially, we obtain the ground states according to the regions in the phase plot (see Fig. 2) by using imaginary-time propagation. After calculating the ground state, we evolve it using real-time propagation by quenching the trap strength.

A. Excitation spectrum in region I

1. Excitation spectrum

We present the collective excitation spectrum for the stable case and corresponding eigenvectors in Fig. 3. Here we consider the coupling strengths $k_L = 0.5$ and $\Omega = 2.0$. Figure 3(a) shows only the presence of $\mathrm{Re}(\omega)$ in the eigenspectrum. The above suggests the presence of a phonon mode [27]. The absence of negative and imaginary eigenfrequencies

in the spectrum indicates that the phase is energetically and dynamically stable throughout region I.

We present the eigenvectors corresponding to the eigenspectrum in Figs. 3(b) and 3(c). We have three sets of eigenvectors: $|u_{+1}|^2$ and $|u_{-1}|^2$, $|u_0|^2$ and $|v_0|^2$, and $|v_{+1}|^2$ and $|v_{-1}|^2$. The eigenvectors exhibit in-phase behavior in all components for all wave numbers, which means that $|u_{+1}(q_x)|^2 = |u_{-1}(q_x)|^2$ and $|v_{+1}(q_x)|^2 = |v_{-1}(q_x)|^2$, indicating the presence of densitylike (in-phase) excitations [see Figs. 3(b) and 3(c)]. We demonstrate that both u and v eigenvectors are in-phase. For $q_x \approx 0$, the eigenvector components approach each other, and at $q_x = 0$ they have equal values, signifying the presence of a phonon mode, as mentioned earlier. As anticipated, the eigenspectrum and eigenvectors exhibit the same behavior for other sets of parameters (k_L and Ω) in the same region (region I of Fig. 2) of the k_L-Ω plane. The critical change in the eigenspectrum is that with increasing coupling strengths, the real eigenspectrum widens, similarly to how the eigenvectors also widen after the junction at $q_x = 0$.

2. Dynamical stability

We consider the same coupling parameters $(k_L, \Omega) = (0.5, 2)$ to examine the dynamical behavior of region I, and the interaction strengths are $c_0 = 0.5$ and $c_2 = -0.1$ by solving the GP equations (1a) and (1b). Here we obtain the plane-wave phase as a ground state of the condensate. To understand the stability of the ground state, we quench the trap strength to half and further evolve the condensate. The density of the condensate shows stable breatherlike motion throughout the dynamical evolution [see Figs. 4(a)–4(c)]. In addition, the system density profile is symmetric in nature and does not show any oscillations, as shown in Figs. 4(a)–4(c). Thus, it is clear that the system is not showing polarization behavior, as we expected from the in-phase nature of eigenvectors shown in Figs. 3(b) and 3(c).

In Fig. 5 we plot the total energy of the condensate. In real-time evolution, we quench the trap strength to one-half its original value. Hence, in the beginning, the energy of the condensate starts decreasing. After a while, the energy stabilizes and remains constant throughout the dynamical evolution.
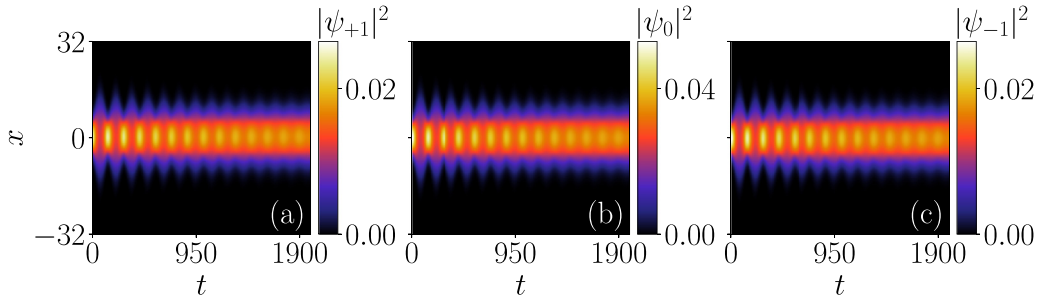
FIG. 4. Time evolution of ground-state density profiles illustrating dynamical stability of the (a) $+1$, (b) 0, and (c) -1 components of the condensate, with the parameters similar to those in Fig. 3. All three components $|\psi_{+1}|^2$, $|\psi_0|^2$, and $|\psi_{-1}|^2$ depict stable breatherlike dynamics, which validates the dynamical stability of the condensate.

Therefore, we find that the ground state of the condensate is energetically and dynamically stable, as shown in the stability phase plot in Fig. 2 corresponding to the excitation spectrum. We also investigate the dynamical spin texture of this region, which does not change its behavior during the dynamical evolution.

B. Excitation spectrum in region IIa

1. Excitation spectrum

To investigate region II, we divide it into two parts, regions IIa and IIb. In the first part we consider two points with fixed SO- and Rabi-coupling strengths $(k_L, \Omega) = (2, 2)$ and $(k_L, \Omega) = (2.35, 4)$, respectively. We plot the dispersion relation of collective excitations and corresponding eigenvectors at these values of the coupling parameters in Fig. 6. Figure 6(a i) shows the presence of the imaginary part of the eigenspectrum at larger values of quasimomentum q_x having two imaginary bands. As we increase the value of Rabi coupling to larger extents than the SO-coupling strength, the two imaginary eigenbands change into a single band [see Fig. 6(a ii)]. It is also shown in Fig. 2, where the second point falls on the boundary of regions I and IIa. Therefore, we can state that the second point is approaching the stable regime.

The eigenvectors corresponding to the eigenenergy is presented in Figs. 6(b) and 6(c). Unlike the behavior observed in
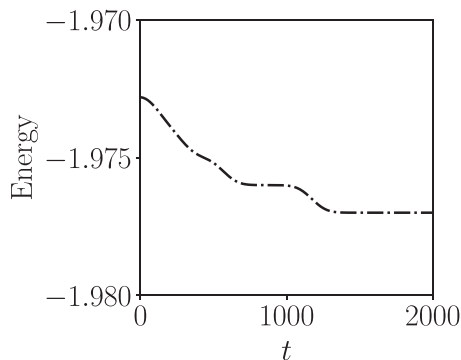

FIG. 5. Energy variation in the time evolution for the stable region I. The parameters are similar to those in Fig. 3. During time evolution, the energy of the condensate decreases in the beginning and further shows stable behavior, which signifies that the condensate is energetically stable due to the lack of negative eigenfrequency.

region I, we find complex behavior in the eigenvector components here. The eigenvector shows in the momentum direction the transition from densitylike (in-phase) excitations, where $|u_{+1}(q_x)|^2 = |u_{-1}(q_x)|^2$ and $|v_{+1}(q_x)|^2 = |v_{-1}(q_x)|^2$, to the spinlike (out-of-phase) excitations, where $|u_{+1}(q_x)|^2 = |v_{-1}(q_x)|^2$ and $|v_{+1}(q_x)|^2 = |u_{-1}(q_x)|^2$. In Fig. 6(a i) the eigenspectrum has double-band instability and corresponding dual transitions from the densitylike mode to the spinlike mode for ± 1 components of eigenvectors. Still, the zeroth component exists only in the densitylike mode. Also, there is an amplitude difference among all three components of the eigenvector; the ± 1 components have half the amplitude value of the zeroth component [see Figs. 6(b i) and 6(c i)]. For the second point in the region [see Fig. 6(a ii)], the eigenspectrum has only single-band instability and corresponding to this, there is a constant transition from the densitylike mode to the spinlike mode of the ± 1 components of eigenvectors [see Fig. 6(b ii)]. The amplitudes of ± 1 and 0 appear to be the same as for the previous point. It is observed from the above discussion that whenever $\text{Im}(\omega_-)$ appears, the densitylike mode [where we have $\text{Re}(\omega_-) = 0$] changes into the spinlike mode. From the transition point of view, when comparing these two points in region IIa, we notice that the multiband instability has mixed densitylike and spinlike mode behavior in the eigenvectors. In detail, by comparing Figs. 6(b i) and 6(b ii), we see that only the latter figure has the densitylike mode in the major portion of the momentum space. However, the former has a mixed type of mode in the same range of momentum space where imaginary eigenvalues appear at $0 < q_x < 2$; it has a spinlike mode when $2 < q_x < 3$ eigenvalues are real and then it exhibits a densitylike mode, for $3 < q_x < 3.5$ again a spinlike mode, and for $q_x > 3.5$ a densitylike mode (the behavior is symmetric about the momentum axis). Such a complex mixed mode has not been explored in the spinor SO-coupled system. We highlight that this study will be helpful for the experimental researcher to achieve the stable ferromagnetic spinor SO-coupled BEC experimentally.

2. Dynamical stability

We divide region II into two parts IIa and IIb. We focus on the system's dynamics in region IIa, specifically at two different points within region IIa. We discuss the dynamic behavior of the system for each point separately. We choose $(k_L, \Omega) = (2, 2)$. We obtain the ground state using imaginary-time
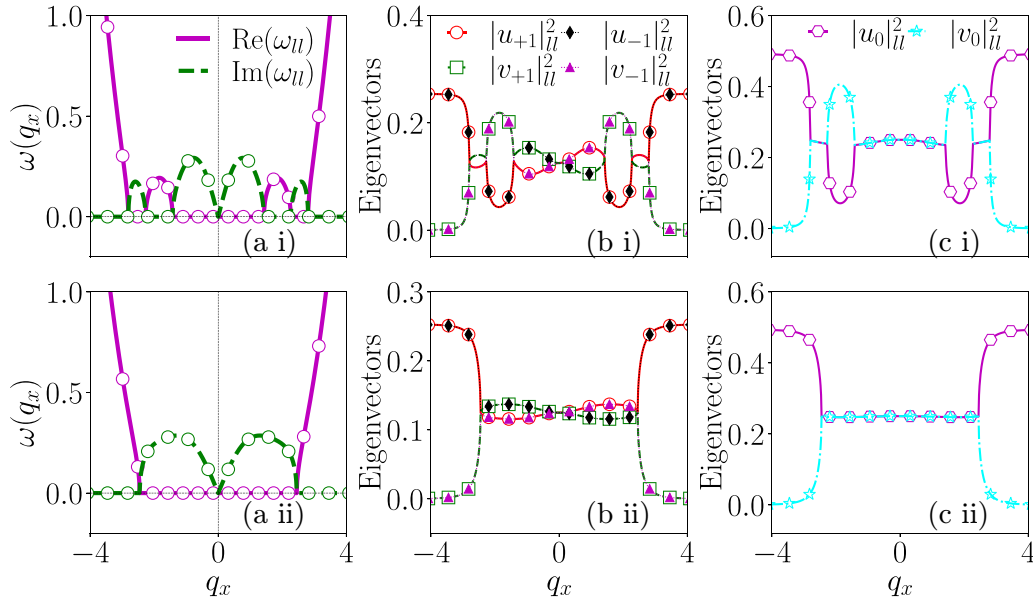
FIG. 6. Stability excitation spectrum eigenvalues and eigenvectors. The SO- and Rabi-coupling strengths are (a i), (b i), and (c i) $(k_L, \Omega) = (2.0, 2.0)$ and (a ii), (b ii), and (c ii) $(2.35, 4.0)$. (a) Eigenenergy and (b) and (c) corresponding eigenvectors. The lines and symbols have the same denotations as in Fig. 3. The eigenenergy spectrum shows the presence of complex eigenfrequencies in terms of (a i) two bands and (a ii) one band, which indicates the system is dynamically unstable. The eigenvectors display the spin dipole along with the spinlike mode in the q_x momentum direction and are symmetric along the axis.

propagation, which is the stripe wave, and evolve the ground state using real-time propagation. The dynamical evolution of the state shows that the stripe wave phase holds up to $t = 150$. Furthermore, the density profile of all three components fragments into nonperiodic domains [see Figs. 7(a)–7(c)] [20]. If the system has a nonvanishing zeroth component in the dynamical evolution, then the system tends to be less subjected to instability. Conversely, if the zeroth component vanishes, the system becomes more prone to instability [60]. In this

case, the appearance of the zeroth component in the dynamical evolution confirms that the chosen coupling point has a lower risk of instability. We plot the total energy of the condensate in Fig. 8(a). The energy of the condensate starts with a value of -2.471. It changes sign from negative to positive at $t = 205$, due to the quench for which a similar kind of agitation happens, and further it shows stable behavior near $t = 365$. At this point, as shown in Fig. 6(a i), the BdG excitation spectrum has complex eigenfrequencies and the eigenvector shows the
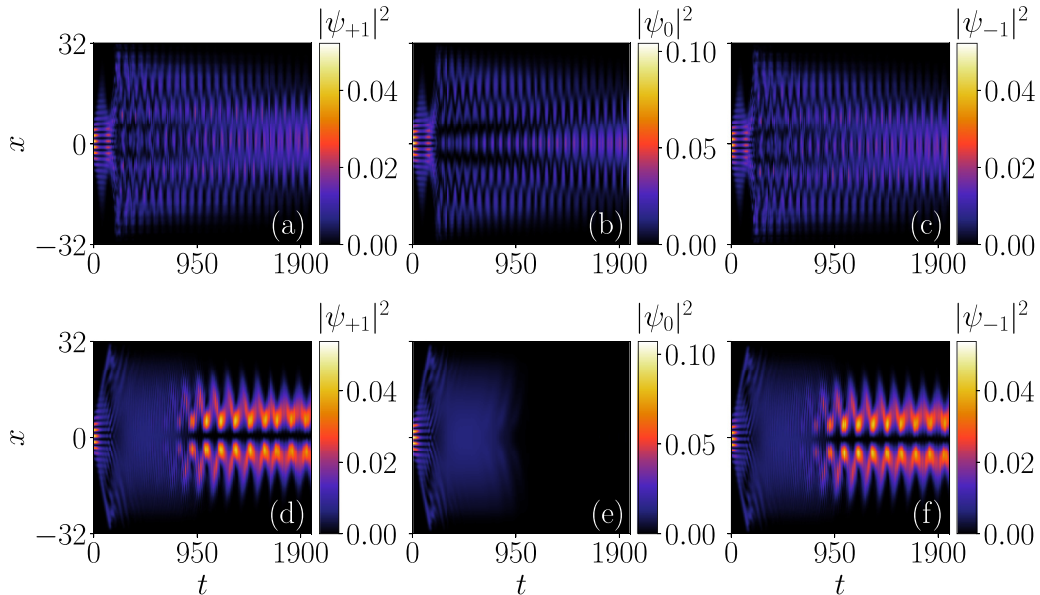

FIG. 7. Temporal evolution of the ground-state density profile of (a) and (d) $|\psi_{+1}|^2$, (b) and (e) $|\psi_0|^2$, and (c) and (f) $|\psi_{-1}|^2$ depicted for different (k_L, Ω): (a)–(c) $(2.0, 2.0)$ and (d)–(f) $(2.35, 4.0)$. The density profile shows stripe wave behavior in both cases for (a)–(c) $t < 150$ and (d)–(f) $t < 180$. Further, it gets fragmented into several small domains. This behavior signifies the change in shape and amplitude of the density profile, where in (d)–(f) the zeroth component loses density while the ± 1 components gain density.
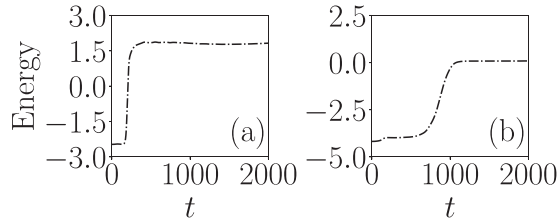
FIG. 8. (a) and (b) Total energy of the condensate for the density evolution in the upper and lower panel of Fig. 7 respectively. In both cases the energy of the condensate increases at the beginning of the dynamical evolution, but finally shows well-settled stable behavior; such a sudden change happens due to the external perturbation. This behavior validates the energetic stability of the condensate; however, the system is dynamically unstable.

out-of-phase behavior for a certain range of quasimomentum. The above indicates that the system is dynamically unstable and generates nonlinear wave patterns, which matches well with numerical simulation results. We choose another point in region IIa at which we consider the value of the SO-coupling strength $k_L = 2.35$ and $\Omega = 4.0$. We achieve the ground state, which is a stripe wave phase. The excitation spectrum has complex eigenfrequencies, as shown in Fig. 6(a ii). The presence of complex eigenfrequencies indicates that the system is dynamically unstable. To verify this claim numerically, we evolve the ground state of the system using the real-time-propagation method as illustrated in Figs. 7(d)–7(f). The stripe wave behavior of the condensate holds its shape for a while. Then it fragments into several small domains [20]. In addition, we observe that with time, the zeroth component of density starts diminishing until it finally disappears [see Fig. 7(e)]. Other components of the condensate density ($|\psi_{\pm 1}|^2$) boost the magnitude after the zeroth component of the density disappears [see Figs. 7(d) and 7(f)]. For the quadratic Zeeman effect, such a dynamical disappearance does not take place [60]. However, in this work we see this sort of dynamical instability in the excitation of spin-1 BECs in the presence of SO coupling alone. So far we have found that the density pattern of the system changes its shape and amplitude with the disappearance of the zeroth component, which is a signature of dynamical instability. Further, we show the total energy of the condensate in Fig. 8(b). It starts from -4.182 and changes its sign from negative to positive at $t = 1080$, which is higher for this point where the zeroth component vanishes, and then the particles are shared by the spin-up and -down components; there the energy gets settled. Such a zeroth component vanishing behavior is not observed for the previous case due to the appearance of spin and density-mixed modes. Upon investigating the dynamical spin texture of this region, we notice that the initial pattern does not maintain its shape as time progresses and changes its spin texture during the dynamical evolution (see Appendix C).

C. Excitation spectrum in region IIb

1. Excitation spectrum

In this part of region II, we choose two different points at which we consider the coupling strengths $k_L = 3.1$ and $\Omega = 1.17$, and $k_L = 5.0$ and $\Omega = 2.5$, respectively. The col-
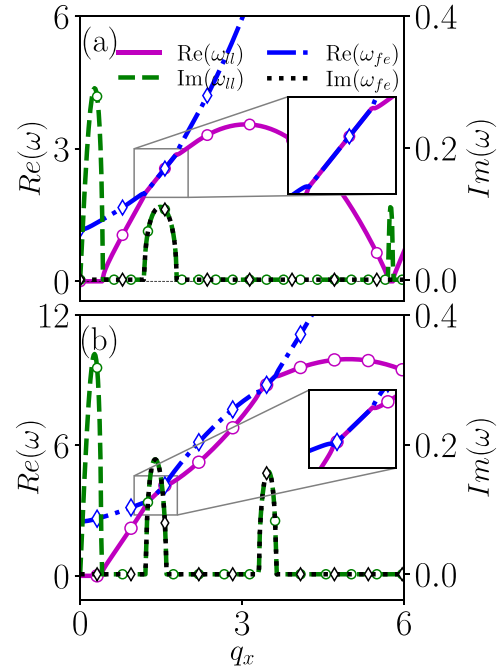

FIG. 9. Excitation spectrum for the coupling strengths (a) $(k_L, \Omega) = (3.1, 1.17)$ and (b) $(k_L, \Omega) = (5.0, 2.5)$ depicting the low-lying and first-excited branches of the spectrum, respectively. The magenta solid line represents $\text{Re}(\omega_-)$ and the green dashed line represents $|\text{Im}(\omega_-)|$, which is the low-lying branch of the spectrum, while the blue dash-dotted line represents $\text{Re}(\omega_+)$ and the black dotted line represents $|\text{Im}(\omega_+)|$, corresponding to the first-excited branch of the spectrum, which is obtained from Eq. (12). The eigenspectrum in (a) and (b) shows multiple instability bands as we obtained in Fig. 6(a i); however, (a) and (b) show one and two modes, corresponding to no gap existing between the lower branch and the first-excited branch. Insets show close-ups of the no-gap mode between the lower and first-excited state branches. The y-axis scale on the right represents the magnitudes of the imaginary eigenfrequencies.

lective excitation spectrum of the condensate for these sets of parameters is given in Fig. 9. We obtain complex eigenfrequencies for both points [see Figs. 9(a) and 9(b)]. Still, the number of instability bands in the quasimomentum direction and its amplitude differ for both points. In Fig. 9(a) the number of low-lying instability bands is 3 and the positions and amplitudes are $\{q_x, \omega\} = \{0.27, 0.29\}$, $\{1.48, 0.11\}$, and $\{5.75, 0.11\}$, respectively. Further, we show the first-excited (ω_{fe}) and low-lying (ω_{ll}) branches of the eigenspectrum, which overlap with each other, where we also find that the complex eigenfrequency is not similar to the eigenspectrum of the previous case of region IIa. This results in modes corresponding to no gap between the first-excited and the low-lying spectrum. However, we find three complex eigenfrequencies in which the overlapping point shows complex eigenfrequencies for both spectra. The phenomenon that is observed in the spinor BECs is related to the unstable avoided crossing between spin and charge modes by considering $\theta = \pi$, the phase difference between the perturbed wave fields, which also provides the class I_o of oscillatory patterns as a result of the dynamical instability [43,44]. However, in this work we
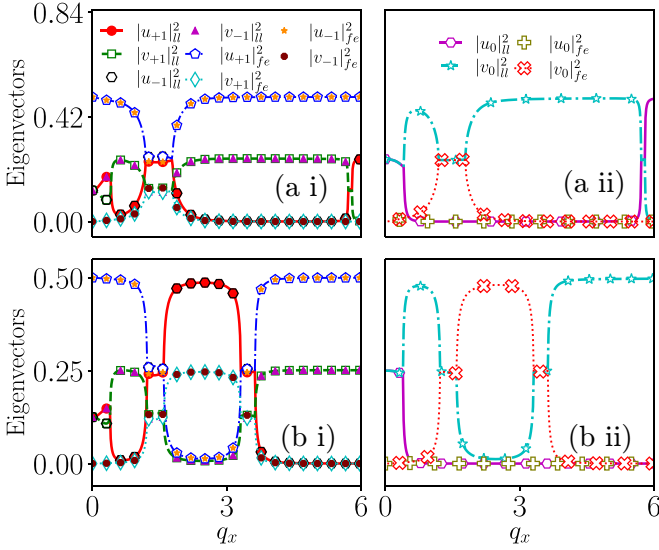
FIG. 10. Eigenvectors in (a) and (b) corresponding to Figs. 9(a) and 9(b), respectively: $|u_{+1}|_{ll}^2$ (closed red circles), $|u_{-1}|_{ll}^2$ (open black hexagons), $|u_0|_{ll}^2$ (open magenta hexagons), $|v_0|_{ll}^2$ (open cyan stars), $|v_{+1}|_{ll}^2$ (open green squares), $|v_{-1}|_{ll}^2$ (closed magenta triangles), $|u_{+1}|_{fe}^2$ (open blue pentagons), $|u_{-1}|_{fe}^2$ (closed orange stars), $|u_0|_{fe}^2$ (open olive pluses), $|v_0|_{fe}^2$ (open red crosses on dotted lines), $|v_{+1}|_{fe}^2$ (open cyan diamonds), and $|v_{-1}|_{fe}^2$ (closed maroon circles). For q_x the eigenfrequencies and eigenvectors are symmetric about the axis. Here we find that the eigenvectors show the spinlike mode when the complex frequency exhibits the densitylike mode only when it is real.

realize the same phenomenon only for the symmetric case $\theta = 0$, even though we consider only SO and Rabi couplings without Raman detuning. Due to the I_o dynamical instability, we find out-of-equilibrium dynamics in the density patterns and it is the route to the formation of nonlinear patterns, which we discuss later in this section. In Fig. 9(b) the number of instability bands is 4 and the positions and amplitudes are $\{q_x, \omega\} = \{0.27, 0.33\}$, $\{1.39, 0.18\}$, $\{3.48, 0.16\}$, and $\{9.45, 0.11\}$ (not shown in figure), respectively. The appearance of instability bands for both points is symmetric about the momentum (q_x) axis. In addition to this, we show the first-excited state in the same plot. Here the first-excited and low-lying branches overlap twice, where we observe two unstable avoided crossings in SO-coupled spinor ferromagnetic BECs. For this case, the first-excited spectrum also has two complex eigenfrequencies for the unstable avoided-crossing points.

The eigenvectors corresponding to the eigenspectrum in Figs. 9(a) and 9(b) are shown in Figs. 10(a) and 10(b), respectively. For the choice of parameters $(k_L, \Omega) = (3.1, 1.17)$, we observe no overlap between the low-lying and the first-excited spectrum eigenvectors. However, the gap between them closes and the overlap happens for certain values of quasimomentum q_x. In the interval $q_x = (-0.4, 0.4)$, where the low-lying spectrum exhibits imaginary eigenvalues, the eigenvectors correspond to the spinlike mode, as we see from the out-of-phase behavior between the low-lying eigenvectors. Further, when $q_x > \pm 0.4$ up to the gapless point, we notice that the low-lying eigenvectors display the densitylike (in-phase) mode. However, the first-excited state only has a

densitylike mode up to this gapless point. Nevertheless, in the region of the spectrum where the low-lying and first-excited branches overlap, we see that the eigenvectors of both the low-lying and first-excited states are out of phase. When the mode corresponding to no gap between the low-lying branch and the first-excited-state branch transforms as a gapped mode, all the eigenvectors are in phase [see Fig. 10(a i)], where the zeroth component shows only a densitylike mode [see Fig. 10(a ii)].

For the second point of this region, all eigenvector components have the same amplitude value. Choosing the coupling parameters $(k_L, \Omega) = (5, 2.5)$ reveals a substantial difference. With these parameters, we observed double overlaps between the low-lying and the first-excited spectrum, closing the gap between them. These overlaps occur for certain values of quasimomentum q_x. The first two eigenvectors exhibit behavior similar to that observed at the previous point.

As the mode corresponding to no gap between the low-lying and first-excited-state branch transforms into a gapped mode, all the eigenvectors become in phase. We also observe a similar feature for the next no-gap mode and further momentum directions. Additionally, we find that when the real eigenvalues fall to zero and then increase, the eigenvectors are flipped but remain in phase, as shown in Fig. 10(a i). The obvious change in the spectrum from the gapped mode to the mode corresponding to no gap between the low-lying and the first-excited-state branch of the eigenvectors demonstrates the transition from a constant densitylike mode to a hybridized spinlike-density mode [61] [see Figs. 10(b i) and 10(b ii)].

2. Dynamical stability

We consider the points $(k_L, \Omega) = (3.1, 1.17)$, with interaction parameters $c_0 = 0.5$ and $c_2 = -0.1$. The collective excitation spectrum corresponding to this point is shown in Fig. 9(a), which has complex eigenfrequencies in terms of multiple bands. The presence of complex eigenfrequencies makes the system dynamically unstable. To verify that the system is dynamically unstable, we perform numerical simulation. We obtain the ground state, which is the stripe wave phase. We evolve the ground state by quenching the trap, and during dynamical evolution, the density profile initially maintains a stripe wave behavior. After a while, the ± 1 components fragment into small domains and show nonperiodic oscillation in space-time evolution, shown in the density profiles in Figs. 11(a) and 11(c). On the other hand, the zeroth component of density starts diminishing as time progresses [see Fig. 11(b)]. Thus, we state that the density pattern of the condensate changes its shape and amplitude during dynamical evolution, which confirms the dynamical instability as the zeroth component disappears due to the instability of the system [60]. We investigate the second point by choosing $(k_L, \Omega) = (5, 2.5)$. For this we obtain the ground state as the stripe wave and evolve the ground state numerically. The dynamical evolution of this phase shows that the stripe wave phase holds for a while. Further, the density profile of all three components fragments into nonperiodic domains [see Figs. 11(d)–11(f)] [20]. Also, the density of the zeroth component starts diminishing, explicitly showing that the system maintains dynamical instability. We also observe that
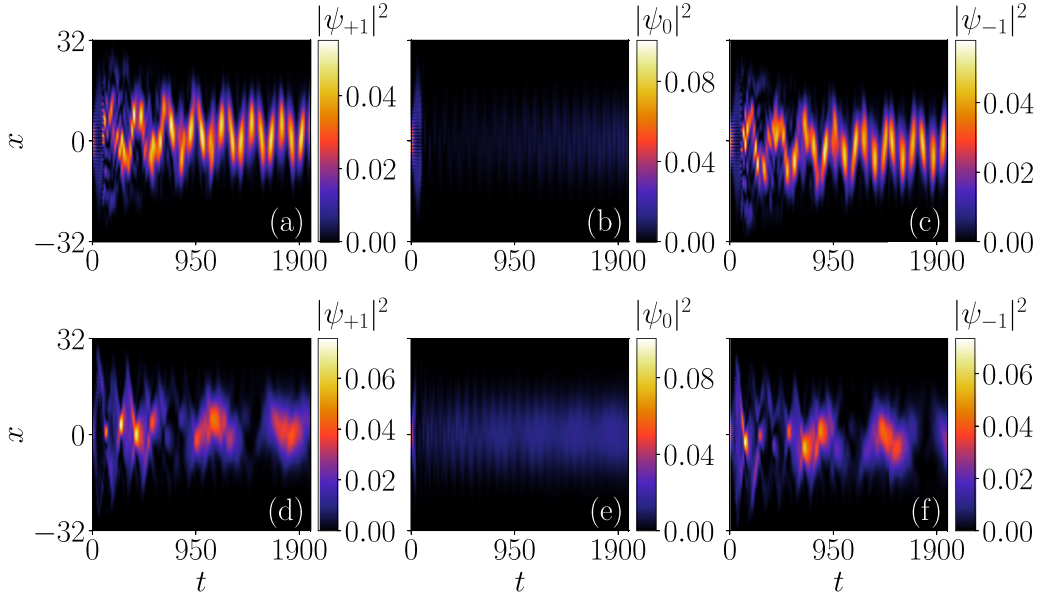
FIG. 11. Dynamics of the ground-state density profile of (a) and (d) $|\psi_{+1}|^2$, (b) and (e) $|\psi_0|^2$, and (c) and (f) $|\psi_{-1}|^2$ components for different (k_L, Ω): (a)–(c) (3.1, 1.17) and (d)–(f) (5.0, 2.5). The density profile has stripe wave behavior in both cases for (a)–(c) $t < 100$ units and (d)–(f) $t < 50$ units. For $t > 100$, (a)–(c) show nonperiodic oscillation and nonuniform density in space-time, whereas the zeroth component disappears. For $t > 50$, (d)–(f) show that the density profile further fragments into several small domains. This behavior signifies the change in shape and amplitude of the density profile, along with the disappearance of the zeroth component, which confirms the dynamical instability.

the density pattern of the system changes its shape and amplitude during dynamical evolution.

We plot the total energy of the condensate in Fig. 12. The ground-state energy of the condensate starts with the values $E_0 = -4.845$ [Fig. 12(a)] and $E_0 = -12.593$ [Fig. 12(b)]. It changes sign from negative to positive (and then is stable) after the sudden change in the parameter during time evolution. We observe that the second point is more energetic than the first point in both the ground state and the excited state, i.e., $E_{\text{ex}} \approx 0.432$ [Fig. 12(a)] and $E_{\text{ex}} \approx 1.708$ [Fig. 12(b)]. Further, we investigate the dynamical spin texture, where the initial pattern is not observed and at the final time it changes its spin texture in the dynamical evolution (see Appendix C).

D. Excitation spectrum in region III

1. Excitation spectrum

In region III we choose points along the horizontal axis to understand the system's behavior in the absence of Rabi-coupling strength $\Omega = 0$ and we consider the SO-coupling strength as $k_L = 5.0$. The collective excitation spectrum for

this is demonstrated in Figs. 13(a) and 13(b), where, differently from the previous cases, in region III we observe the presence of roton-maxonlike modes. As demonstrated in previous studies [34,36,62], when $\Omega \to 0$ the roton-maxon

FIG. 13. (a) Low-lying and (b) first-excited branches of the excitation spectrum for the coupling strengths $k_L = 5.0$ and $\Omega = 0.0$. The lines and symbols have the same denotations as in Fig. 9. Insets show close-ups of the complex frequency modes. The mode corresponding to no gap between the low-lying- and first-excited-state branches appears along with the symmetric roton mode.
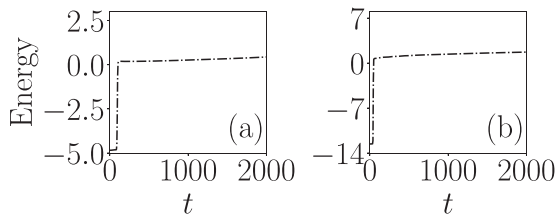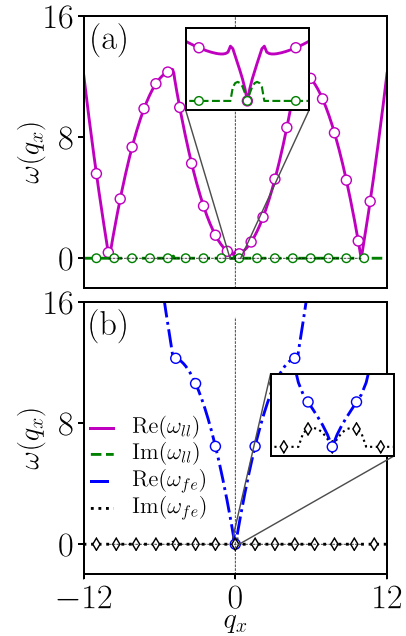

FIG. 12. Total energies of the condensate for the dynamical evolution from Fig. 11. From the energy saturation, we understand that the system is energetically stable but dynamically unstable.
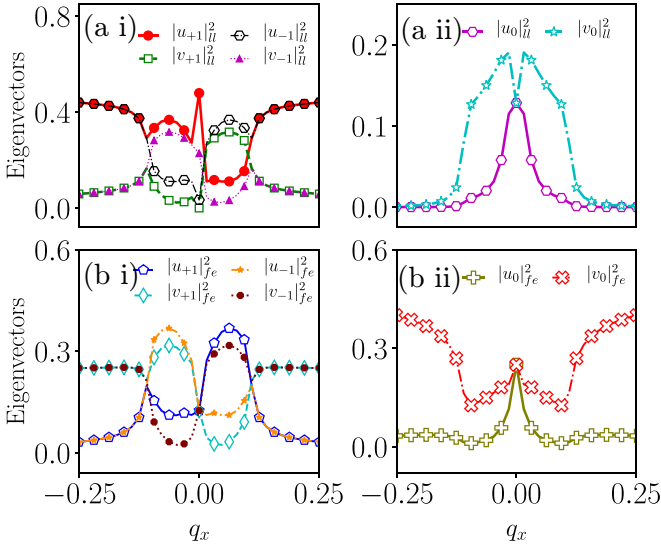
FIG. 14. Eigenvectors in (a) and (b) corresponding to Figs. 13(a) and 13(b), respectively. The lines and symbols have the same denotations as in Fig. 10. In this region, both the low-lying and first-excited states assume the value $\omega = 0$ for $q_x = 0$ with eigenvectors that are in phase with the low-lying and first-excited states, which indicates the existence of the phonon mode for these branches.

modes appear and the roton mode subsequently softens when Ω approaches zero. The softening of the roton mode favors the appearance of superstripe structures. The low-lying excitation has complex eigenfrequencies along with the phonon and symmetric rotonlike modes, indicating that the system is dynamically unstable due to the presence of the imaginary eigenfrequencies. Further, the first-excited state also shows similar behavior, i.e., the presence of the phonon mode along with the complex eigenfrequencies but no symmetric rotonlike structure. However, the unstable avoided crossing is noticed at $q_x \approx 4.8499$, between the first-excited and low-lying states. After that point, the real eigenfrequency decreases and reaches zero, where it exhibits the imaginary eigenfrequency. Beyond this point, the real frequency grows. Based on this observation, one has to understand such behavior using the eigenvectors. Additionally, the complex eigenfrequency presents multiple instability bands along the quasimomentum axis. The positions of the instability bands of the low-lying excitation spectrum are $q_x = 0.06, 4.91, 9.97$ and the corresponding complex eigenfrequencies are $\omega_- = 0.1037, 0.1404, 0.0993$, respectively. The first-excited state has two instability bands and its position and complex eigenfrequency are the same as those of the low-lying state. Notably, the instability bands are symmetric about the x axis.

Figure 14 represents the eigenvector components; in this region, the low-lying excitation eigenvectors exhibit an in-phase mode between $|u_{+1}|^2_{ll}$ and $|u_{-1}|^2_{ll}$ and between $|v_{+1}|^2_{ll}$ and $|v_{-1}|^2_{ll}$. This feature continues up to the point of real eigenvalues, when the imaginary eigenvalues exhibit an out-of-phase mode between them ($|u_{+1}|^2_{ll} - |u_{-1}|^2_{ll} \neq 0$). Even though at $q_x = 0$ the eigenvalues become zero $\omega = 0$, a phonon mode is observed, which is explicitly shown in the form of sharp spikelike eigenvectors appearing in $|u_{+1}|^2_{ll}$

and $|v_{+1}|^2_{ll}$. However, in this complex eigenvalue regime, we have both the phonon mode and the complicated spinlike mode. In addition to this, the zeroth component eigenvectors show a mixed-mode behavior; as a result, we observe different dynamical phases from the ground state. Also, the first-excited state exhibits $\omega = 0$ for $q_x = 0$, where all the eigenvectors meet at a single point, as before. The first-excited state behaves like a spinlike mode with an asymmetric nature, indicating the existence of the superstripe phase. Further, the density mode appears while the real eigenfrequency is present, which is also evident from the zeroth component eigenvector behavior.

2. Dynamical stability

We consider a case with SO-coupling strength $k_L = 5.0$ and Rabi-coupling strength $\Omega = 0.0$. The corresponding BdG excitation spectra in Figs. 13(a) and 13(b) reveal the presence of phonon-gapless complex eigenfrequencies, indicating the dynamical unstable nature of the condensate. To investigate this numerically, we obtain the ground state of the condensate, which falls within the unpolarized stripe wave phase. We then evolve this state in time using a real-time-propagation method. The density profile initially maintains its unpolarized stripe wave behavior but subsequently breaks into two parts at $t = 85$. Following this, the density of ± 1 components oscillates around the trap center, exhibiting accumulated breather behavior for a period. Ultimately, the fragmented oscillating waves merge and form several small domains [see Figs. 15(a) and 15(c)] [20], while the zeroth component of the density disappears [see Fig. 15(b)]. This behavior signifies that the dynamical instability also changes its shape and size [60]. We examine the energy during its dynamic evolution, which eventually stabilizes, indicating energetic stability. This finding is consistent with the analysis of the excitation spectrum, suggesting that the numerical simulation accurately reflects the theoretical predictions.

E. Effect of coupling strength on the band gap

So far, we have discussed the nature of collective excitations, eigenvectors, and the dynamical behavior of the condensate in different regions of the k_L-Ω plane. Next we consider the effect of the SO- and Rabi-coupling strengths on the band gap Δ_g between the positive and negative branches of the spectrum, where we define the band gap as Δ_g. In Fig. 16(a i) we show the band-gap variation upon varying the Rabi-coupling strength Ω for a fixed k_L. In what follows we discuss band-gap variation for two distinct SO coupling strengths, for instance, $k_L = 1.14$ and 3.10. The gap closes at a certain value of Ω for these SO couplings. For $k_L = 1.14$, $\Delta_g = 0$ for $\Omega = 0.107$ and similarly for $k_L = 3.10$, it closes at $\Omega = 1.218$ for the quasimomentum values $q = 0.521$ and 1.486, respectively. Starting from the point $\Delta_g = 0$, upon increasing the Ω, we observe that the gap becomes nonzero even for a relatively small increment in the Rabi-coupling strength and the magnitude of the band gap increases with an increase in Ω. Also, we provide the logarithmic scale plot corresponding to Fig. 16(a i), where we show the fitting curve $\Delta_g = a\Omega^b$ with the maroon and orange dotted lines for $k_L = 1.14$ and 3.10, respectively. The coefficients for the fitting function are
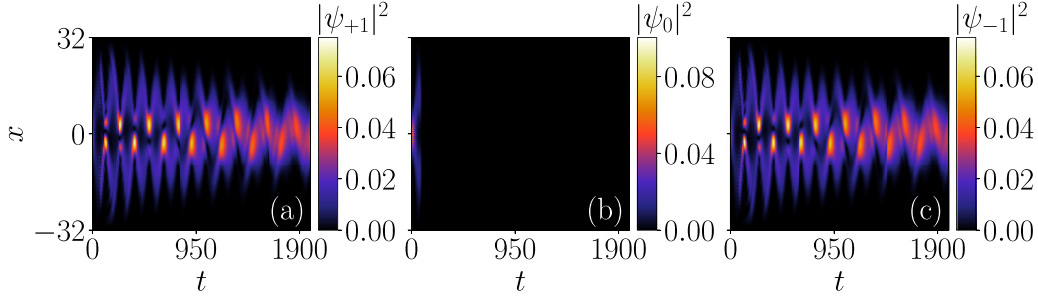
FIG. 15. Time evolution of superstripe ground-state density profiles of the (a) $|\psi_{+1}|^2$, (b) $|\psi_0|^2$, and (c) $|\psi_{-1}|^2$ components of the condensate. The coupling strengths are $k_L = 5.0$ and $\Omega = 0.0$ with interaction parameters $c_0 = 0.5$ and $c_2 = -0.1$. Throughout the dynamics, the unpolarized superstripe wave holds its behavior for $t < 30$. Further, it breaks into two domains and oscillates on either side of the condensates of ± 1 components. The zeroth component disappears, where ± 1 components gain density, which shows the change in the density profile confirms the dynamical instability.

$a = 0.981$ and $b = 0.997$, and $a = 1.083$ and $b = 1.026$ for the SO-coupling strengths $k_L = 1.14$ and 3.10, respectively. Here we wish to highlight that the band gap increases upon increasing Ω for fixed k_L. For higher k_L, the gap attains a sudden maximum even for the lesser Ω for small k_L, which is evident where the red dashed line crosses the green dash-dotted line in Fig. 16(a i). Moreover, for higher k_L the gap closes at higher Ω; compare starting points in Fig. 16(a i).
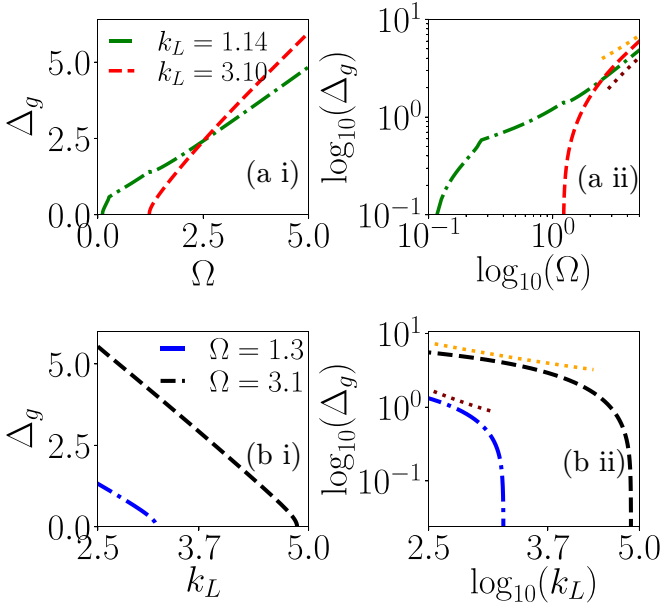

FIG. 16. Variation of the band gap Δ_g between negative and positive branches of the spectrum for (a i) the fixed value SO coupling strength upon variation of the Rabi-coupling strength and (b i) vice versa. (a i) The green dash-dotted line and the red dashed line represent gap calculations for $k_L = 1.14$ and 3.10, respectively. (b i) The blue dash-dotted line and the black dashed line represent gap calculations for $\Omega = 1.3$ and 3.1, respectively. The interaction parameter strengths are $c_0 = 0.5$ and $c_2 = -0.1$. (a ii) and (b ii) Logarithmic scale plots corresponding to (a i) and (b i), respectively. In (a ii) and (b ii) the maroon (orange) dotted lines represent the fitting curve $\Delta_g = a\Omega^b$ with the parameters $a = 0.9811$ and $b = 0.9974$ ($a = 1.0825$ and $b = 1.0258$) and $a = 126.2992$ and $b = -4.9568$ ($a = 46.4438$ and $b = -2.2146$), respectively.

Further, we discuss the variation of the band gap upon varying the SO coupling for fixed Rabi-coupling strength. We choose two different values of Rabi-coupling strength $\Omega = 1.3, 3.1$. Since the Rabi-coupling strength is responsible for opening the gap among the branches of the collective excitation spectrum (as discussed above), the band-gap value Δ_g is higher for a lesser value of k_L at fixed Ω [see Fig. 16(b i)]. Upon increasing k_L, the Δ_g starts decreasing, and further it reaches zero at the quasimomentum values $q_x = 1.5325, 2.3381$ with $k_L = 3.20, 4.86$ for the Rabi-coupling strengths $\Omega = 1.3, 3.1$, respectively. We find that the band gap Δ_g decreases upon increasing k_L at fixed Ω. In Fig. 16(b ii) we show the fitting function $\Delta_g = c\Omega^d$ with the maroon and orange dotted lines for $\Omega = 1.3$ and 3.1, respectively. The coefficients of fitting functions are $c = 126.30$ and $d = -4.96$, and $c = 46.44$ and $d = -2.22$ for the SO-coupling strengths $\Omega = 1.3$ and $k_L = 3.1$, respectively.

VI. CONCLUSION

In this paper we have investigated the collective excitation spectrum of SO-coupled spin-1 ferromagnetic BECs with Rabi coupling in quasi-one-dimension using the Bogoliubov–de Gennes theory and numerical simulation. We analyzed the single-particle spectrum for different sets of SO- and Rabi-coupling strengths. Upon increasing the strength of coupling parameters, we noticed separation among different negative (ω_-) and positive (ω_+) branches of the eigenspectrum, with ω_- having the lowest minimum. However, for $\Omega < k_L^2$, the negative branch of the spectrum shows a double minimum, indicating the presence of a stripe phase.

Based upon the collective excitation calculation, we obtained the phase diagram in the k_L-Ω plane which was broadly divided into three regions: region I (a stable phase) and regions II and III (unstable phases). We divided the unstable region II into two parts according to the nature of the eigenspectrum, which is based upon the appearance of the gapped and gapless (unstable avoided-crossing) modes. In region I, the excitation spectrum exhibits solely real positive eigenvalues with the presence of a phonon mode. The eigenvectors corresponding to these eigenvalues substantiate the existence of the phonon mode by exhibiting the density-like mode in the wave-number space. The absence of

negative and complex eigenfrequencies in the spectrum confirms a dynamically and energetically stable condensate in this region.

As the coupling strengths increase, we found a transition from region I to the unstable region II, attributed to the relation $\Omega < k_L^2$. In this region, complex eigenfrequencies emerge throughout the spectrum, accompanied by a gapped mode and a mode corresponding to no gap between the low-lying (ω_-) and first-excited (ω_+) branches. Based on the presence of a gapped mode and a mode corresponding to no gap between the low-lying- and first-excited-state branches, region II is divided into two parts IIa and IIb, respectively. The eigenspectrum in region IIa exhibits gapped behavior across the entire region. Notably, the presence of complex eigenfrequencies is reflected in the corresponding eigenvectors, indicating a transition from a spin-mode nature to a density-mode nature of the eigenvectors as the eigenfrequency shifts from complex to real. This phenomenon is evident in the ± 1 components of the eigenspectrum, while the zeroth component exclusively displays a densitylike mode. The combined analysis of eigenvectors and dynamic behavior reveals a mixed spin-density mode.

Region IIb is separated from region IIa by a line; the latter region exhibits a multi-instability band across its entirety. Upon increasing the SO coupling for a point along the separation line, we observe gapless behavior in the eigenspectrum for a particular range of quasimomentum among the low-lying and first-excited branches of the spectrum. Similarly, decreasing the Rabi-coupling strength for any point on the separation line will also yield gapless behavior. Similar to the previous region, we also identify the mixed spin-density eigenvector mode in this region. For the gapless region, the eigenvector of the low-lying and first-excited branches exhibits a spinlike mode for all its components. We also characterize the mode corresponding to no gap between the low-lying- and the first-excited-state branch as an unstable avoided crossing between the low-lying and first-excited spectrum. This instability manifests as the emergence of complex eigenfrequencies when the two branches come into contact. The corresponding dynamical evolution also exhibits an unstable stripe state, which we examined numerically. We observed that the zeroth component is nonzero in region IIa but disappears in region IIb. This suggests that a nonzero zeroth component tends to be less susceptible to dynamical instability, while a vanishing zeroth component tends to be higher than the previous one.

In addition to these two regions, we identified region III, which corresponds to the $\Omega = 0$ line. In this region, both the low-lying and the first-excited states assume the value $\omega = 0$ for $q_x = 0$ with eigenvectors in phase with the low-lying state. This indicates the existence of a phonon mode. The low-lying and first-excited spectra also exhibit gapless, unstable avoided-crossing behavior between them. Further analysis of the eigenvectors reveals not only the phonon character but also the presence of a spinlike mode in both states. Numerical simulations for this case reveal the presence of a superstripe ground state, and their respective dynamics exhibit unstable dynamical nonlinear patterns. Our observations suggest that this work would be a valuable resource for experimental researchers seeking to achieve stable and unstable SO-coupled spinor ferromagnetic BECs. Here we have provided a comprehensive numerical simulation of regions with diverse dynamical behaviors.

In this work we found the absence of the plane-wave phase in the excitation spectrum. In recent studies it was shown that in the presence of the Zeeman coupling the double degeneracy in the excitation spectrum is eliminated and hence the plane-wave phase appears [36,37]. We would be interested in extending the present work in the presence of the Zeeman field to explore the effect of the field on the nature of the overall eigenspectrum and eigenvectors. Another interesting feature that has emerged in the SO-coupled BECs is the appearance of a self-bound quantum droplet in the binary BECs [63,64] in which the repulsive nature of the mean-field interaction is balanced by the beyond-mean-field quantum fluctuation in one dimension [64,65]. It would be interesting to extend the present work of SO-coupled spin-1 BECs considering the effect of quantum fluctuation on different phases of the collective excitation modes along similar lines as presented for spin-1/2 SO-coupled BECs [66].

APPENDIX A: RELEVANT TERMS OF THE BDG MATRIX OF COLLECTIVE EXCITATIONS

In this Appendix we provide an explicit form of the matrix elements of the BdG matrix (10) used in Sec. V. The matrix elements of Eq. (10) read

$$H_+ = \frac{q_x^2}{2} + c_0\left(2\phi_{+1}^2 + \phi_0^2 + \phi_{-1}^2\right) + c_2\left(2\phi_{+1}^2 + \phi_0^2 - \phi_{-1}^2\right), \tag{A1a}$$

$$H_0 = \frac{q_x^2}{2} + c_0\left(\phi_{+1}^2 + 2\phi_0^2 + \phi_{-1}^2\right) + c_2\left(\phi_{+1}^2 + \phi_{-1}^2\right), \tag{A1b}$$

$$H_- = \frac{q_x^2}{2} + c_0\left(\phi_{+1}^2 + \phi_0^2 + 2\phi_{-1}^2\right) + c_2\left(2\phi_{-1}^2 + \phi_0^2 - \phi_{+1}^2\right), \tag{A1c}$$

$$\mu_+\phi_{+1} = c_0(\phi_{+1}^2 + \phi_0^2 + \phi_{-1}^2)\phi_{+1} + c_2(\phi_{+1}^2 + \phi_0^2 - \phi_{-1}^2)\phi_{+1} + c_2\phi_0^2\phi_{-1}^* + \frac{\Omega}{\sqrt{2}}\phi_0, \tag{A1d}$$

$$\mu_0\phi_0 = c_0(\phi_{+1}^2 + \phi_0^2 + \phi_{-1}^2)\phi_0 + c_2(\phi_{+1}^2 + \phi_{-1}^2)\phi_0 + 2c_2\phi_0^*\phi_{+1}\phi_{-1} + \frac{\Omega}{\sqrt{2}}(\phi_{+1} + \phi_{-1}), \tag{A1e}$$

$$\mu_-\phi_{-1} = c_0(\phi_{+1}^2 + \phi_0^2 + \phi_{-1}^2)\phi_{-1} + c_2(\phi_{-1}^2 + \phi_0^2 - \phi_{+1}^2)\phi_{-1} + c_2\phi_0^2\phi_{+1}^* + \frac{\Omega}{\sqrt{2}}\phi_0, \tag{A1f}$$

$$\mathcal{L}_{12} = C^+\phi_{+1}^2, \quad \mathcal{L}_{13} = C^+\phi_0^*\phi_{+1} - \frac{k_L}{\sqrt{2}}iq_x + 2c_2\phi_0\phi_{-1}^* + \frac{\Omega}{\sqrt{2}}, \quad \mathcal{L}_{14} = C^+\phi_0\phi_{+1}, \quad \mathcal{L}_{15} = C^-\phi_{-1}^*\phi_{+1},$$

$$\mathcal{L}_{16} = C^-\phi_{-1}\phi_{+1} + c_2\phi_0^2, \quad \mathcal{L}_{21} = -C^+\phi_{+1}^{*2}, \quad \mathcal{L}_{23} = -C^+\phi_0^*\phi_{+1}^*, \quad \mathcal{L}_{24} = -C^+\phi_0\phi_{+1}^* + \frac{k_L}{\sqrt{2}}iq_x - 2c_2\phi_0^*\phi_{-1} - \frac{\Omega}{\sqrt{2}},$$

$$\mathcal{L}_{25} = -C^-\phi_{-1}^*\phi_{+1}* - c_2\phi_0^{*2}, \quad \mathcal{L}_{26} = -C^-\phi_{-1}\phi_{+1}^*, \quad \mathcal{L}_{31} = C^+\phi_{+1}^*\phi_0 + 2c_2\phi_0^*\phi_{-1} + \frac{k_L}{\sqrt{2}}iq_x + \frac{\Omega}{\sqrt{2}}, \quad \mathcal{L}_{32} = C^+\phi_{+1}\phi_0,$$

$$\mathcal{L}_{34} = c_0\phi_0^2 + 2c_2\phi_{+1}\phi_{-1}, \quad \mathcal{L}_{35} = C^+\phi_{-1}^*\phi_0 + 2c_2\phi_0^*\phi_{+1} - \frac{k_L}{\sqrt{2}}iq_x + \frac{\Omega}{\sqrt{2}}, \quad \mathcal{L}_{36} = C^+\phi_{-1}\phi_0, \quad \mathcal{L}_{41} = -C^+\phi_{+1}^*\phi_0^*,$$

$$\mathcal{L}_{42} = -C^+\phi_{+1}\phi_0^* - \frac{k_L}{\sqrt{2}}iq_x - 2c_2\phi_0\phi_{-1}^* - \frac{\Omega}{\sqrt{2}}, \quad \mathcal{L}_{43} = -c_0\phi_0^{*2} - 2c_2\phi_{+1}^*\phi_{-1}^*, \quad \mathcal{L}_{45} = -C^+\phi_{-1}^*\phi_0^*,$$

$$\mathcal{L}_{46} = -C^+\phi_{-1}\phi_0^* + \frac{k_L}{\sqrt{2}}iq_x - 2c_2\phi_0\phi_{+1}^* - \frac{\Omega}{\sqrt{2}}, \quad \mathcal{L}_{51} = C^-\phi_{+1}^*\phi_{-1}, \quad \mathcal{L}_{52} = C^-\phi_{+1}\phi_{-1} + c_2\phi_0^2,$$

$$\mathcal{L}_{53} = C^+\phi_0^*\phi_{-1} + \frac{k_L}{\sqrt{2}}iq_x + 2c_2\phi_0\phi_{+1}^* + \frac{\Omega}{\sqrt{2}}, \quad \mathcal{L}_{54} = C^+\phi_0\phi_{-1}, \quad \mathcal{L}_{56} = C^+\phi_{-1}^2, \quad \mathcal{L}_{61} = -C^-\phi_{+1}^*\phi_{-1}^* - c_2\phi_0^{*2},$$

$$\mathcal{L}_{62} = -C^-\phi_{+1}\phi_{-1}^*, \quad \mathcal{L}_{63} = -C^+\phi_0^*\phi_{-1}^*, \quad \mathcal{L}_{64} = -C^+\phi_0\phi_{-1}^* - \frac{k_L}{\sqrt{2}}iq_x - 2c_2\phi_0^8\phi_{+1} - \frac{\Omega}{\sqrt{2}}, \quad \mathcal{L}_{65} = -C^+\phi_{-1}^{*2}.$$

Also,

$$C^+ \equiv c_0 + c_2, \quad C^- \equiv c_0 - c_2.$$

The coefficients for the BdG characteristic equation (12) are

$$b = -5\Omega^2 - 4c_2^2 - (2k_L^2 + 3\Omega + c_0)q_x^2 - \frac{3}{4}q_x^4 + c_2(8\Omega + q_x^2), \tag{A2}$$

$$c = 4\Omega^4 + \Omega\left[2\Omega(k_L^2 + 3\Omega) - (k_L^2 - 5\Omega)c_0\right]q_x^2 + 4c_2^3q_x^2 + \frac{1}{2}\left[2k_L^4 + 9\Omega^2 + (k_L^2 + 6\Omega)c_0\right]q_x^4 + \frac{1}{2}(3\Omega + c_0)q_x^6$$
$$+ \frac{3}{16}q_x^8 + 4c_2^2\left[\Omega^2 + (k_L^2 - \Omega + c_0)q_x^2\right] - \frac{1}{2}c_2\left[16\Omega^3 + 2\Omega(7k_L^2 + 5\Omega + 8c_0)q_x^2 + (k_L^2 + 6\Omega + 4c_0)q_x^4 + q_x^6\right], \tag{A3}$$

$$d = -\frac{1}{64}q_x^2\left[(4k_L^2 - 4\Omega - q_x^2)(2\Omega + q_x^2) + c_2(-8k_L^2 + 8\Omega + 4q_x^2)\right]\left\{-4c_0\left[8\Omega^2 - 2(k_L^2 - 3\Omega)q_x^2 + q_x^4 - 4c_2(2\Omega + q_x^2)\right]\right.$$
$$\left. + (2\Omega + q_x^2)\left[-16\Omega c_2 + 16c_2^2 - q_x^2(-4k_L^2 + 4\Omega + q_x^2)\right]\right\}. \tag{A4}$$

APPENDIX B: PHASE DIAGRAM FOR DIFFERENT INTERACTION STRENGTHS

Here we present a detailed phase diagram in the k_L-Ω plane for interaction strengths other than $c_0 = 0.5$ and $c_2 = -0.1$, as considered in this work. For $c_0 = 0.5$ and $c_2 = -0.1$ we have mainly observed three different regions, on the basis of the collective excitation spectrum. Based on the above observations, here we show such a phase diagram for two other different sets of interaction strengths $c_0 = 5.0$ and $c_2 = -0.1$, and $c_0 = 885.72$ and $c_2 = -4.09$. In Fig. 17(a) we show the stability phase diagram in the k_L-Ω plane for the interaction strengths $c_0 = 5$ and $c_2 = -0.1$. The stability phase diagram has been obtained by solving Eq. (10) and analyzing the collective excitation spectrum for these set of parameters. The

phase diagram shows the presence of a stable region (region I) and an unstable region (region II), which is given using the relation $k_L^2 = \Omega$. Region II has been divided into two parts: region IIa and region IIb. The transition line that separates regions IIa and IIb is given using the relation $\Omega = 0.134k_L^2 - 0.0668$, where we observed that only the boundary can be changed; otherwise three regions are found. The gapless behavior emerges after the points $k_L^c = 0.72$ and $\Omega^c = 0.001$, which is also the origin of the line that separates regions IIa and IIb. At the horizontal line at which $\Omega = 0.0$, we obtain a phonon mode in the low-lying and in the first-excited branch of the spectrum, along with the presence of an instability band, which is different from previous regions. The cutoff value of SO-coupling strength to obtain this behavior along the line is $k_L = 0.96$.
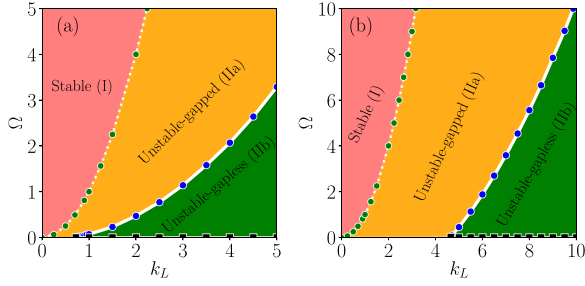
FIG. 17. Phase diagram in the k_L-Ω plane for interaction parameters (a) $c_0 = 5.0$ and $c_2 = -0.1$ and (b) $c_0 = 885.72$ and $c_2 = -4.09$. Based on the different characteristics of the eigenspectrum and ground state, the phase diagram is divided into regions I, IIa, IIb, and III. Region I is stable, while regions IIa and IIb are unstable. The line $\Omega = k_L^2$ is drawn, separating region I from II. Blue dots separate regions IIa and IIb. The horizontal line with $\Omega \sim 0$ denotes region III. The behavior of all the regions remains the same as for $c_0 = 0.5$ and $c_2 = -0.1$.

Figure 17(b) illustrates a similar stability phase diagram for the k_L-Ω plane, featuring a very high interaction parameter strength for the interaction parameters $c_0 = 885.72$ and $c_2 = -4.09$. Both real and complex eigenfrequencies coexist with a gapped mode and a mode corresponding to no gap between the low-lying- and first-excited-state branches for this set of interaction strengths. Varying the strengths of the spin-orbit and Rabi couplings allows us to observe the transition from the stable region (region I) to the unstable region (region II) in the phase diagram. The relationship $k_L^2 = \Omega$ defines the boundary between region I and region II. The transition line that separates regions IIa and IIb is given by the relation $\Omega = 0.1317 k_L^2 - 2.8512$. The origin points of the line are $k_L^c = 4.65$ and $\Omega^c = 0.02$. We treat the horizontal line along which the Rabi-coupling strength is zero as region III, where the cutoff value of SO coupling to achieve this behavior is $k_L = 8.1$.

APPENDIX C: SPIN-MAGNETIZATION DENSITY VECTORS

The spatial distribution (or orientation) of spin magnetization density vectors can be referred to as spin texture [67]. Comparing the spin textures at the initial and finite times, we have characterized the dynamical behavior of the stable (region I) and unstable regions (IIa, IIb, and III) in a systemic way. The relevant quantities for the characterization, that is, the spin magnetization density vectors, are defined as

$$m_x = \text{Re}[\sqrt{2}(\psi_{+1} + \psi_{-1})^* \psi_0], \tag{C1a}$$

$$m_y = \text{Im}[\sqrt{2}(\psi_{+1} - \psi_{-1})^* \psi_0], \tag{C1b}$$

$$m_z = |\psi_{+1}|^2 - |\psi_{-1}|^2. \tag{C1c}$$

In Fig. 18 we show the components of the magnetization vector computed using Eqs. (C1a)–(C1c) for two sets of coupling parameters of the dynamically unstable region IIa of the k_L-Ω plane as depicted in Fig. 2. We show the magnetization profile at two instants of time $t = 0$ (for the ground state) and at later instant $t = 1000$ for $k_L = 2.0$ and $\Omega = 2.0$ [see Figs. 18(a i), 18(b i), and 18(c i)] and the same for other parameters $k_L = 2.35$ and $\Omega = 4.0$ [see Figs. 18(a ii), 18(b ii), and 18(c ii)]. For both cases, the entire magnetic component profile exhibits significant changes at a later time ($t = 1000$) compared to those for the ground state, confirming the dynamical instability of the condensate for these sets of coupling parameters in region IIa. This trend continues for another set of points in region IIa. A similar trend of the magnetization vector component profile has been observed for the two sets of coupling parameters $k_L = 3.1$ and $\Omega = 1.17$, and $k_L = 5.0$ and $\Omega = 2.5$ of region IIb, as depicted in the Figs. 19(a i), 19(b i), and 19(c i) and Figs. 19(a ii), 19(b ii), and 19(c ii), respectively.
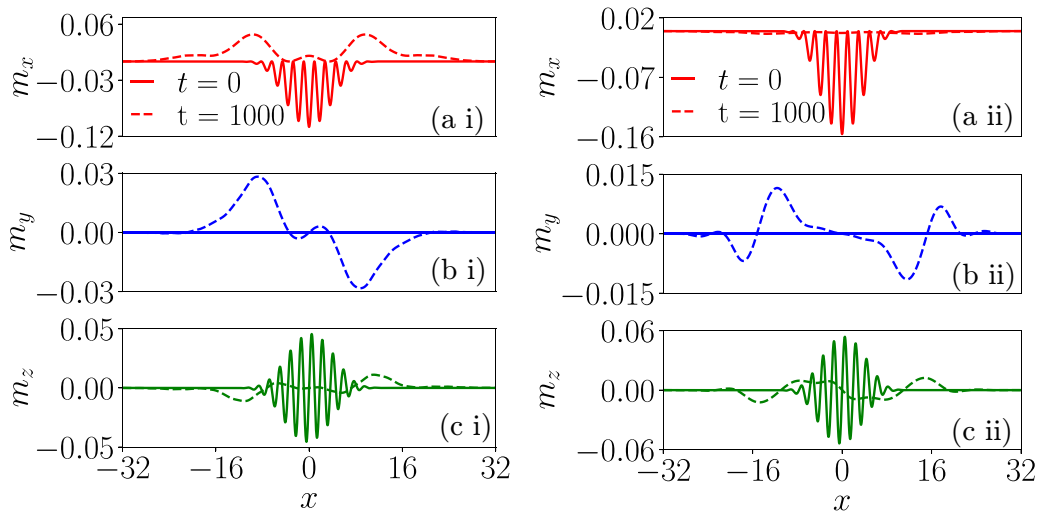

FIG. 18. Spin-magnetization density components (m_x, m_y, m_z) for the ground state at initial time $t = 0$ (solid line) and later time $t = 1000$ (dashed line) in the dynamically unstable region IIa in the k_L-Ω plane for different sets of coupling parameters of the condensate with ferromagnetic interactions $c_0 = 0.5$ and $c_2 = -0.1$: (a i), (b i), and (c i) $k_L = 2.0$ and $\Omega = 2.0$ and (a ii), (b ii), and (c ii) $k_L = 2.35$ and $\Omega = 4.0$. Owing to the dynamical instability, the spin texture deviates from its initial state during the time evolution.
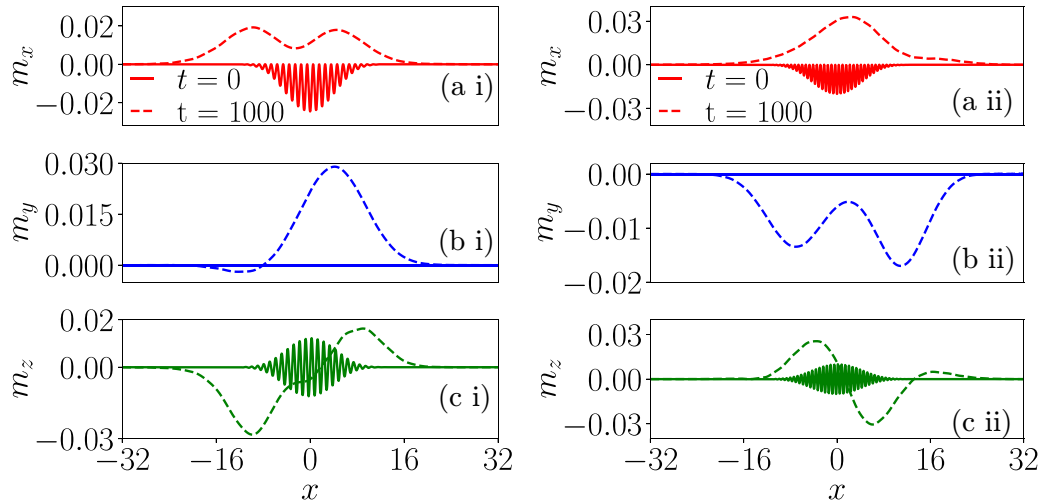
FIG. 19. Spatial profile of the spin-magnetization density components (m_x, m_y, m_z) for the ground state at initial time $t = 0$ (solid line) and later time $t = 1000$ (dashed line) in the dynamically unstable region IIb in the k_L-Ω plane for different sets of coupling parameters of the condensate with ferromagnetic interactions $c_0 = 0.5$ and $c_2 = -0.1$: (a i), (b i), and (c i) $k_L = 3.1$ and $\Omega = 1.17$ and (a ii), (b ii), and (c ii) $k_L = 5.0$ and $\Omega = 2.5$. Owing to the dynamical instability, spin texture shows a deviation from the initial behavior during the time evolution.

[1] Y. Zhang, M. E. Mossman, T. Busch, P. Engels, and C. Zhang, Front. Phys. **11**, 118103 (2016).

[2] D. Jacob, L. Shao, V. Corre, T. Zibold, L. De Sarlo, E. Mimoun, J. Dalibard, and F. Gerbier, Phys. Rev. A **86**, 061601(R) (2012).

[3] D. Campbell, R. Price, A. Putra, A. Valdés-Curiel, D. Trypogeorgos, and I. Spielman, Nat. Commun. **7**, 10897 (2016).

[4] K. Kasamatsu, M. Tsubota, and M. Ueda, Int. J. Mod. Phys. B **19**, 1835 (2005).

[5] K. Fujimoto and M. Tsubota, Phys. Rev. A **85**, 033642 (2012).

[6] Z.-Q. Yu, Phys. Rev. A **93**, 033648 (2016).

[7] G. I. Martone, F. V. Pepe, P. Facchi, S. Pascazio, and S. Stringari, Phys. Rev. Lett. **117**, 125301 (2016).

[8] G.-Q. Li, G.-D. Chen, P. Peng, Z. Li, and X.-D. Bai, J. Phys. B: At. Mol. Opt. Phys. **50**, 235302 (2017).

[9] B. A. Malomed, Europhys. Lett. **122**, 36001 (2018).

[10] P. Peng, G.-Q. Li, L.-C. Zhao, W.-L. Yang, and Z.-Y. Yang, Phys. Lett. A **383**, 2883 (2019).

[11] S. Adhikari, J. Phys.: Condens. Matter **33**, 265402 (2021).

[12] S. Gautam and S. K. Adhikari, Phys. Rev. A **90**, 043619 (2014).

[13] S. K. Adhikari, Phys. Rev. A **100**, 063618 (2019).

[14] S. Gautam and S. K. Adhikari, Laser Phys. Lett. **12**, 045501 (2015).

[15] S. K. Adhikari, Physica E **118**, 113892 (2020).

[16] S. Gautam and S. Adhikari, Braz. J. Phys. **51**, 298 (2021).

[17] S. Mardonov, M. Modugno, and E. Y. Sherman, Phys. Rev. Lett. **115**, 180402 (2015).

[18] S. Mardonov, V. V. Konotop, B. A. Malomed, M. Modugno, and E. Y. Sherman, Phys. Rev. A **98**, 023604 (2018).

[19] S. Mardonov, M. Modugno, E. Y. Sherman, and B. A. Malomed, Phys. Rev. A **99**, 013611 (2019).

[20] T. Mithun and K. Kasamatsu, J. Phys. B: At. Mol. Opt. Phys. **52**, 045301 (2019).

[21] J. Cabedo, J. Claramunt, and A. Celi, Phys. Rev. A **104**, L031305 (2021).

[22] Q.-L. Zhu, L. Pan, and J. An, Phys. Rev. A **102**, 053320 (2020).

[23] Y.-J. Lin, K. Jiménez-García, and I. B. Spielman, Nature (London) **471**, 83 (2011).

[24] R. Ravisankar, T. Sriraman, R. K. Kumar, P. Muruganandam, and P. K. Mishra, J. Phys. B: At. Mol. Opt. Phys. **54**, 225301 (2021).

[25] E. V. Goldstein and P. Meystre, Phys. Rev. A **55**, 2935 (1997).

[26] W. Zhang, D. L. Zhou, M.-S. Chang, M. S. Chapman, and L. You, Phys. Rev. Lett. **95**, 180403 (2005).

[27] C. J. Pethick and H. Smith, *Bose-Einstein Condensation in Dilute Gases*, 2nd ed. (Cambridge University Press, Cambridge, 2008).

[28] L. Pitaevskii and S. Stringari, *Bose-Einstein Condensation and Superfluidity* (Oxford University Press, Oxford, 2016).

[29] N. Bogoliubov, J. Phys. (USSR) **11**, 23 (1947).

[30] D. S. Jin, J. R. Ensher, M. R. Matthews, C. E. Wieman, and E. A. Cornell, Phys. Rev. Lett. **77**, 420 (1996).

[31] M.-O. Mewes, M. R. Andrews, N. J. van Druten, D. M. Kurn, D. S. Durfee, C. G. Townsend, and W. Ketterle, Phys. Rev. Lett. **77**, 988 (1996).

[32] G. I. Martone, Y. Li, L. P. Pitaevskii, and S. Stringari, Phys. Rev. A **86**, 063621 (2012).

[33] Y. Li, G. I. Martone, L. P. Pitaevskii, and S. Stringari, Phys. Rev. Lett. **110**, 235302 (2013).

[34] M. A. Khamehchi, Y. Zhang, C. Hamner, T. Busch, and P. Engels, Phys. Rev. A **90**, 063624 (2014).

[35] L. Chen, H. Pu, Z.-Q. Yu, and Y. Zhang, Phys. Rev. A **95**, 033616 (2017).

[36] Y. Chen, H. Lyu, Y. Xu, and Y. Zhang, New J. Phys. **24**, 073041 (2022).

[37] J. He and J. Lin, New J. Phys. **25**, 093041 (2023).

[38] T. Ozawa, L. P. Pitaevskii, and S. Stringari, Phys. Rev. A **87**, 063610 (2013).

[39] R. Ravisankar, H. Fabrelli, A. Gammal, P. Muruganandam, and P. K. Mishra, Phys. Rev. A **104**, 053315 (2021).

[40] G. Katsimiga, S. Mistakidis, P. Schmelcher, and P. Kevrekidis, New J. Phys. **23**, 013015 (2021).

[41] G. C. Katsimiga, S. I. Mistakidis, K. Mukherjee, P. G. Kevrekidis, and P. Schmelcher, Phys. Rev. A **107**, 013313 (2023).

[42] Rajat, A. Roy, and S. Gautam, Phys. Rev. A **106**, 013304 (2022).

[43] M. C. Cross and P. C. Hohenberg, Rev. Mod. Phys. **65**, 851 (1993).

[44] N. R. Bernier, E. G. Dalla Torre, and E. Demler, Phys. Rev. Lett. **113**, 065303 (2014).

[45] L. Salasnich, A. Parola, and L. Reatto, Phys. Rev. A **65**, 043614 (2002).

[46] S. K. Adhikari, Phys. Rev. E **104**, 024207 (2021).

[47] Y. Kawaguchi and M. Ueda, Phys. Rep. **520**, 253 (2012).

[48] D. M. Stamper-Kurn and M. Ueda, Rev. Mod. Phys. **85**, 1191 (2013).

[49] R. Ravisankar, D. Vudragović, P. Muruganandam, A. Balaž, and S. K. Adhikari, Comput. Phys. Commun. **259**, 107657 (2021).

[50] S. Inouye, M. Andrews, J. Stenger, H.-J. Miesner, D. M. Stamper-Kurn, and W. Ketterle, Nature (London) **392**, 151 (1998).

[51] A. Marte, T. Volz, J. Schuster, S. Dürr, G. Rempe, E. G. M. van Kempen, and B. J. Verhaar, Phys. Rev. Lett. **89**, 283202 (2002).

[52] C. Chin, R. Grimm, P. Julienne, and E. Tiesinga, Rev. Mod. Phys. **82**, 1225 (2010).

[53] L. Wen, Q. Sun, H. Q. Wang, A. C. Ji, and W. M. Liu, Phys. Rev. A **86**, 043602 (2012).

[54] K. Rajaswathi, S. Bhuvaneswari, R. Radha, and P. Muruganandam, Phys. Rev. A **108**, 033317 (2023).

[55] C. Wang, C. Gao, C.-M. Jian, and H. Zhai, Phys. Rev. Lett. **105**, 160403 (2010).

[56] Q. Zhu, C. Zhang, and B. Wu, Europhys. Lett. **100**, 50003 (2012).

[57] E. Anderson, Z. Bai, C. Bischof, L. S. Blackford, J. Demmel, J. Dongarra, J. Du Croz, A. Greenbaum, S. Hammarling, A. McKenney *et al.*, *LAPACK Users' Guide* (SIAM, Philadelphia, 1999).

[58] P. Muruganandam and S. K. Adhikari, Comput. Phys. Commun. **180**, 1888 (2009).

[59] L. E. Young-S., D. Vudragović, P. Muruganandam, S. K. Adhikari, and A. Balaž, Comput. Phys. Commun. **204**, 209 (2016).

[60] R. S. Tasgal and Y. B. Band, Phys. Rev. A **91**, 013615 (2015).

[61] M. Abad and A. Recati, Eur. Phys. J. D **67**, 148 (2013).

[62] H. Lyu and Y. Zhang, Phys. Rev. A **102**, 023327 (2020).

[63] C. R. Cabrera, L. Tanzi, J. Sanz, B. Naylor, P. Thomas, P. Cheiney, and L. Tarruell, Science **359**, 301 (2018).

[64] D. S. Petrov, Phys. Rev. Lett. **115**, 155302 (2015).

[65] S. Gangwar, R. Ravisankar, P. Muruganandam, and P. K. Mishra, Phys. Rev. A **106**, 063315 (2022).

[66] S. Gangwar, R. Ravisankar, S. I. Mistakidis, P. Muruganandam, and P. K. Mishra, Phys. Rev. A **109**, 013321 (2024).

[67] L. Sadler, J. Higbie, S. Leslie, M. Vengalattore, and D. Stamper-Kurn, Nature (London) **443**, 312 (2006).